

## Getting the most from the statistical analysis of solar neutrino oscillations

G. L. Fogli,<sup>1</sup> E. Lisi,<sup>1</sup> A. Marrone,<sup>1</sup> D. Montanino,<sup>2</sup> and A. Palazzo<sup>1</sup>

<sup>1</sup>*Dipartimento di Fisica and Sezione INFN di Bari, Via Amendola 173, 70126 Bari, Italy*

<sup>2</sup>*Dipartimento di Scienza dei Materiali and Sezione INFN di Lecce, Via Arnesano, 73100 Lecce, Italy*

(Received 25 June 2002; published 30 September 2002)

We present a thorough analysis of the current solar neutrino data, in the context of two-flavor active neutrino oscillations. We aim at performing an accurate and exhaustive statistical treatment of both the input and the output information. Concerning the input information, we analyze 81 observables, including the total event rate from the chlorine experiment, the total gallium event rate and its winter-summer difference, the 44 bins of the Super-Kamiokande (SK) energy-nadir electron spectrum, and the 34 day-night energy spectrum bins from the Sudbury Neutrino Observatory (SNO) experiment. We carefully evaluate and propagate the effects of 31 sources of correlated systematic uncertainties, including 12 standard solar model (SSM) input errors, the  $^8\text{B}$  neutrino energy spectrum uncertainty, as well as 11 and 7 systematics in SK and SNO, respectively. Concerning the output information, we express the  $\chi^2$  analysis results in terms of “pulls,” embedding the single contributions to the total  $\chi^2$  coming from both the observables and the systematics. It is shown that the pull method, as compared to the (numerically equivalent) covariance matrix approach, is not only simpler and more advantageous, but also includes useful indications about the preferred variations of the neutrino fluxes with respect to their SSM predictions. Our final results confirm the current best-fit solution at large mixing angle (LMA), but also allow, with acceptable statistical significance, other solutions in the low-mass (LOW) or in the quasivacuum oscillation (QVO) regime. Concerning the LMA solution, our analysis provides conservative bounds on the oscillation parameters, and shows that the contribution of correlated systematics to the total  $\chi^2$  is rather modest. In addition, within the LMA solution, the allowed variations from SSM neutrino fluxes are presented in detail. Concerning the LOW and QVO solutions, the analysis of the pull distributions clearly shows that they are still statistically acceptable, while the small mixing angle (SMA) solution could be recovered only by *ad hoc* “recalibrations” of several SSM and experimental systematics. A series of Appendixes elucidate various topics related to the  $\chi^2$  statistics, the winter-summer difference in GALLEX-GNO, the treatment of the SK and SNO spectra, and a quasi-model-independent comparison of the SK and SNO total rates.

DOI: 10.1103/PhysRevD.66.053010

PACS number(s): 26.65.+t, 13.15.+g, 14.60.Pq, 91.35.-x

### I. INTRODUCTION

The data from the Homestake [1], SAGE [2], GALLEX-GNO [3,4], Kamiokande [5], Super-Kamiokande (SK) [6], and Sudbury Neutrino Observatory (SNO) [7–9] experiments have consistently established that electron neutrinos emitted from the Sun [10] undergo flavor transitions to the other active states ( $\nu_\mu$  or  $\nu_\tau$ ). Neutrino oscillations [11], possibly affected by matter effects in the Sun or in the Earth [12], represent a beautiful explanation of such transitions.

Assuming the simplest scenario of two-family oscillations among active neutrinos, an important task for the next future is to refine the current constraints on the neutrino squared mass difference  $\delta m^2 = m_2^2 - m_1^2 > 0$  and on the mixing angle  $\theta_{12} \in [0, \pi/2]$ . In order to accomplish this task, one needs: (a) new or more precise measurements; (b) accurate calculations of the  $\nu_e$  survival probability  $P_{ee}(\delta m^2, \theta_{12})$  and of related observable quantities; and (c) powerful statistical analyses to compare the (increasingly large) solar  $\nu$  data set with theoretical expectations.

The point (a), not discussed in this work, will soon be addressed by the decisive reactor  $\bar{\nu}_e$  experiment KamLAND [13], as well as by the solar  $\nu$  experiments which are currently running [2,4,9], being restored [6], or in construction [14]. Concerning the point (b), since the current numerical

and analytical understanding of the oscillation probability (and related observables) is quite mature in the whole  $(\delta m^2, \theta_{12})$  plane, we will only make a few remarks when needed. In this paper, we rather focus on point (c), aiming at an exhaustive statistical analysis including all known observables and uncertainties in input, and providing very detailed information in output, in order to better appreciate the current status of the solutions to the solar  $\nu$  problem in terms of active flavor oscillations. Although some details will be specific of solar  $\nu$  data, the analysis method that we discuss is quite general, and can be easily extended to any kind of global fit.

The structure of our paper is the following. In Sec. II we discuss the equivalence between the  $\chi^2$  approaches in terms of the covariance matrix and of “pulls” of observables and systematics. In Sec. III we describe the input and output of the pull approach, as applied to the analysis of 81 solar neutrino observables and of 31 input systematics, in the context of 2  $\nu$  active oscillations. In Sec. IV we discuss the  $\chi^2$  analysis results in terms of multiple allowed regions in the mass-mixing parameter space  $(\delta m^2, \tan^2 \theta_{12})$  and in terms of the associated pull distributions, which provide additional information about the relative likelihood of the various solutions and about the allowed deviations from standard solar model (SSM) fluxes. We draw our conclusions in Sec. V. More technical (but sometimes substantial) issues are discussed in

a series of Appendixes, which deal with the  $\chi^2$  statistics (Appendix A), the winter-summer asymmetry in GALLEX-GNO (Appendix B), the treatment of the SK spectrum uncertainties (Appendix C), the analysis of the SNO data (Appendix D), and a quasi-model-independent comparison of SK and SNO total rates (Appendix E).

As a conclusion to this Introduction, we would like to stress that deepening the statistical analysis and improving the evaluation of the uncertainties is an important task in neutrino oscillation physics, just as it happens (or happened) in other areas of “precision” physics. Indeed, after the observation of two large oscillation effects (the disappearance of atmospheric  $\nu_\mu$  and of solar  $\nu_e$ , and their upcoming tests at long-baseline accelerator and reactor experiments), we are likely to face an era of delicate searches for smaller effects related, e.g., to the angle  $\theta_{13}$ , to leptonic  $CP$  violation, or to subleading contributions induced by nonstandard  $\nu$  states or interactions. Moreover, one should not forget that, so far, there is no *direct* evidence for a vacuum oscillation pattern (disappearance and reappearance of a specific flavor) or for matter effects in the Sun or the Earth. Such effects might well generate only small signals in present or planned experiments, and any effort should be made in order to quantify them (if any) with accurate analyses. From this viewpoint, we think that our thorough analysis can add valuable information and useful technical tools to other solar  $\nu$  fits [6,9,15–20] that appeared soon after the release of the SNO neutral current data [8].

## II. TWO EQUIVALENT WAYS OF DEFINING THE $\chi^2$ FUNCTION

Let us consider a set of  $N$  observables  $\{R_n\}_{n=1, \dots, N}$  with their associated sets of experimental observations  $\{R_n^{\text{expt}}\}$  and theoretical predictions  $\{R_n^{\text{theor}}\}$ . In general, one wants to build a  $\chi^2$  function which measures the differences  $R_n^{\text{expt}} - R_n^{\text{theor}}$  in units of the total (experimental and theoretical) uncertainties. This task is completely determined if, for any difference  $R_n^{\text{expt}} - R_n^{\text{theor}}$ , one can estimate an uncorrelated error  $u_n$ , and a set of  $K$  correlated systematic errors  $c_n^k$  induced by  $K$  independent sources, namely

$$R_n^{\text{expt}} - R_n^{\text{theor}} \pm u_n \pm c_n^1 \pm c_n^2 \dots \pm c_n^K \quad (n=1, \dots, N), \quad (1)$$

with

$$\rho(u_n, u_m) = \delta_{nm}, \quad (2)$$

$$\rho(c_n^k, c_m^h) = \delta_{kh} \mathbf{V}(n, m), \quad (3)$$

where  $\rho$  represents the correlation index.<sup>1</sup>

<sup>1</sup>The error  $c_n^k$  represents the shift of the  $n$ -th observable induced by a  $+1\sigma$  variation in the  $k$ -th systematic error source. Linear propagation of errors is assumed, namely, possible  $\pm 1\sigma$  asymmetries and second-order systematic effects  $\propto c_n^k c_n^h$  are consistently neglected in computing the uncertainties of the difference  $R_n^{\text{expt}} - R_n^{\text{theor}}$ .

Given the input numbers in Eq. (1), two  $\chi^2$  definitions have been basically used in global analyses (with some variants or combinations). They will be referred to as the “covariance” approach (Sec. II A) and the “pull” approach (Sec. II B). Although seemingly different, the two approaches are strictly equivalent (Sec. II C). The pull approach, however, proves to be much more advantageous, and will be used throughout this paper.

### A. The covariance approach

In the “covariance approach,” one builds the (covariance) matrix of squared errors as

$$\sigma_{nm}^2 = \delta_{nm} u_n u_m + \sum_{k=1}^K c_n^k c_m^k, \quad (4)$$

then inverts it, and evaluates the quadratic form

$$\chi_{\text{covar}}^2 = \sum_{n,m=1}^N (R_n^{\text{expt}} - R_n^{\text{theor}}) [\sigma_{nm}^2]^{-1} (R_m^{\text{expt}} - R_m^{\text{theor}}). \quad (5)$$

This approach, proposed in [21] for the data available at that time, has been later used in the majority of solar  $\nu$  analyses of total events rates, with some variants related to the treatment of the  $^8\text{B}$   $\nu$  flux (free or SSM) and to the separation of spectral and total rate information in the SK data.

### B. The pull approach

The alternative “pull approach” embeds the effect of each independent  $k$ -th source of systematics through a shift of the difference  $R_n^{\text{expt}} - R_n^{\text{theor}}$  by an amount  $-\xi_k c_n^k$ , where  $\xi_k$  is a univariate Gaussian random variable<sup>2</sup>

$$(R_n^{\text{expt}} - R_n^{\text{theor}}) \rightarrow (R_n^{\text{expt}} - R_n^{\text{theor}}) - \sum_{k=1}^K \xi_k c_n^k. \quad (6)$$

The normalization condition for the  $\xi_k$ 's is implemented through quadratic penalties in the  $\chi^2$ , which is then minimized with respect to all  $\xi_k$ 's,

$$\chi_{\text{pull}}^2 = \min_{\{\xi_k\}} \left[ \sum_{n=1}^N \left( \frac{R_n^{\text{expt}} - R_n^{\text{theor}} - \sum_{k=1}^K \xi_k c_n^k}{u_n} \right)^2 + \sum_{k=1}^K \xi_k^2 \right]. \quad (7)$$

Denoting as  $\bar{\xi}_k$  (“pulls” of the systematics) the values of the  $\xi_k$ 's at the minimum, and defining the “pulls”  $x_n$  of the observables as

<sup>2</sup>The minus sign preceding the terms  $\xi_k c_n^k$  is conventional. It amounts to attribute all the shifts to the theoretical estimate:  $R_n^{\text{theor}} \rightarrow R_n^{\text{theor}} + \sum_{k=1}^K \bar{\xi}_k c_n^k$ .

$$\bar{x}_n = \frac{R_n^{\text{expt}} - \left( R_n^{\text{theor}} + \sum_{k=1}^K \bar{\xi}_k c_n^k \right)}{u_n}, \quad (8)$$

the value of  $\chi_{\text{pull}}^2$  is then split into two diagonalized pieces, embedding the contribution to the  $\chi^2$  from the residuals of the observables and of the systematics,

$$\chi_{\text{pull}}^2 = \chi_{\text{obs}}^2 + \chi_{\text{sys}}^2 \quad (9)$$

$$= \sum_{n=1}^N \bar{x}_n^2 + \sum_{k=1}^K \bar{\xi}_k^2. \quad (10)$$

The pull approach has often been used by the SK Collaboration in their day-night spectral analysis, in combination with the covariance method for non-SK data [22]. More recently, the SK energy-nadir spectrum has been analyzed through a mixed pull-covariance approach [23]. The link between the covariance and pull method, discussed in the next section, is also mentioned in passing in Ref. [24]. To our knowledge, however, a complete analysis of solar neutrino data in terms of  $\chi_{\text{pull}}^2$  has not been performed, prior to the present work.

### C. Comparison and equivalence of the covariance and pull approaches

It is perhaps not generally known that, although seemingly different, the covariance and pull approaches are strictly equivalent,

$$\chi_{\text{covar}}^2 \equiv \chi_{\text{pull}}^2. \quad (11)$$

Our proof of the above identity is given in Appendix A.<sup>3</sup> Given the equivalence in Eq. (11), the choice between the covariance and the pull approach must be dictated by their relative merits.

In particle physics, the covariance approach is typically used either when the experimental collaborations provide detailed information about the correlation matrix (as in the case of the CERN  $e^+e^-$  collider LEP Electroweak Working Group [30]), or when  $N \ll K$  (as in the case of solar neutrino fits to total rates only [21]). However, for increasing  $N$  the approach becomes increasingly complicated. The inversion of large  $N \times N$  covariance matrices, in addition to being numerically tricky, can make it difficult to fully understand the results of global analyses. Indeed, the current solar or atmospheric neutrino data fits, involving  $N \sim \mathcal{O}(10^2)$ , are getting close to their manageability limits in terms of covariance

<sup>3</sup>We have recently realized that Eq. (11) and its implications have been also discussed [25] and are routinely used [26,27] in the context of parton density distribution fitting [28]. Closely related results have also been recently found in the context of cosmic microwave background data fitting [29]. Although the connection between covariance matrix and pulls appears thus to be an ubiquitous result in physics data analysis, we have been unable to trace explicit references to Eq. (11) prior to Ref. [25].

matrices. The situation might become even more problematic in future high-statistics experiments, such as the neutrino factories from muon storage rings or superbeams, where the oscillation parameters will be inferred from the analysis and comparison of densely binned and correlated (anti)neutrino event spectra.<sup>4</sup>

The pull approach is clearly more practical than the covariance one when  $K \ll N$ . In fact, the minimization in Eq. (7) leads to a set of  $K$  linear equations in the  $\bar{\xi}_k$ 's, and to an associated  $K \times K$  matrix inversion, rather than the  $N \times N$  covariance matrix inversion (see Appendix A). Moreover, the final decomposition in terms of pulls of observables and systematics [Eqs. (9) and (10)] allows to trace the *individual* contributions to the  $\chi^2$ , and to easily detect anomalously large residuals. Indeed, the pull distribution has been recognized as a useful diagnostic tool in many areas of physics, including electroweak precision physics [30] and, more recently, solar  $\nu$  physics, as discussed in [32] (see also [19]).<sup>5</sup> In general, this method is useful to gauge the mutual agreement of data in a global fit, or to diagnose tension among data (if any), for any given point in the model parameter space [ $(\delta m^2, \tan^2 \theta_{12})$  in our case]. The analysis of the  $\chi_{\text{obs}}^2$  and  $\chi_{\text{sys}}^2$  components [Eq. (9)] can also be useful to trace possible sources of good or bad fits.

Given the advantages of  $\chi_{\text{pull}}^2$  in cases where  $K \ll N$ , we have redesigned the statistical analysis of solar neutrino oscillations in terms of pulls, and applied it to the current data set (where  $N=81$  and  $K=31$ ), as discussed in the next section.

## III. INPUT AND OUTPUT FOR THE $\chi_{\text{pull}}^2$ ANALYSIS

In this section we describe the main input and output quantities, related to the  $\chi_{\text{pull}}^2$  analysis of solar neutrino data. In input we consider a set of  $N=81$  observables  $R_n$  (with associated uncorrelated errors  $u_n$ ), and a set of  $K=31$  sources of correlated systematic errors  $c_n^k$ , in part related to the SSM and in part to the experiments.<sup>6</sup> In output we consider the total  $\chi_{\text{pull}}^2$ , its decomposition in individual pulls, and the shifts of the neutrino fluxes from their SSM value.

### A. Input observables and uncorrelated errors

The first two observables in our list are the chlorine total rate [1],

$$R_{\text{Cl}}^{\text{expt}} = 2.56 \pm 0.23 \text{ SNU}, \quad (12)$$

<sup>4</sup>The pull approach has been recently applied to prospective studies in this context [31].

<sup>5</sup>Notice that in Refs. [19,30,32] the pulls are defined in a somewhat different way, namely, without the shifts in Eq. (8).

<sup>6</sup>Systematic error sources are defined as ‘‘correlated’’ if they act upon two or more observables at the same time. Systematics which act upon one observable only (e.g., the  $\nu$ -Cl absorption cross section error) simply contribute quadratically to the uncorrelated error for that observable (the Cl total rate, in the example).

and the average Gallium total rate (SAGE [2] + GALLEX-GNO [4]),

$$R_{\text{Ga}}^{\text{expt}} = 70.8 \pm 4.4 \text{ SNU}, \quad (13)$$

where the errors include the statistical and experimental systematic contributions to the uncorrelated errors  $u_{\text{Cl}}$  and  $u_{\text{Ga}}$ , respectively. In the analysis, the corresponding cross section uncertainties must also be added in quadrature. Following the suggestion in [33], the cross section error components  $\Delta R_{X,i}$  for  $X = (\text{Cl}, \text{Ga})$  are first added linearly and then quadratically into low ( $L$ ) and “high” ( $H$ ) energy parts [ $L = (\text{pp}, \text{pep}, \text{Be}, \text{N}, \text{O})$  and  $H = (\text{B}, \text{hep})$ , respectively]<sup>7</sup>

$$u_X^2(\text{cross section}) = \left( \sum_{i \in L} \Delta R_{X,i}^{\text{theor}} \right)^2 + \left( \sum_{i \in H} \Delta R_{X,i}^{\text{theor}} \right)^2. \quad (14)$$

For  $X = \text{Cl}$ , the cross section error components are evaluated as  $\Delta R_{X,i} = R_{X,i} \Delta \ln C_{X,i}$ , where  $R_{X,i}$  are the (oscillated) rate components, and the fractional  $1\sigma$  cross section uncertainties  $\Delta \ln C_{X,i}$  can be taken from the compilation in [37]. For  $X = \text{Ga}$ , the value of  $\Delta R_{X,i}$  is computed by taking  $1/3$  of the variations induced by the  $\pm 3\sigma$  perturbed cross sections [38] on the  $i$ -th Ga rate component for each point of the oscillation parameter space, as suggested in [33].<sup>8</sup>

Our third observable is the winter-summer ( $W-S$ ) rate difference [39] measured in GALLEX-GNO [4], here introduced for the first time in the oscillation analysis. This datum is described in detail in Appendix B.

The SK experiments provide 44 observables, in terms of (binned) absolute event rates for the energy-nadir differential spectrum of electrons [6]. Our treatment of the SK spectral information is described in detail in Sec. III C.

The set of solar  $\nu$  observables is completed by the 34 day-night energy spectrum bins from the SNO experiment [8,9], which include contributions from  $\nu$  elastic scattering (ES), charged current (CC) and neutral current (NC) interactions, and backgrounds [40]. Our treatment of the SNO spectral information is described in Appendix D.

## B. Input correlated systematics

The 31 sources of correlated systematics include 12 uncertainties related to SSM input, the  ${}^8\text{B}$   $\nu$  energy shape uncertainty, 11 SK error sources and 7 SNO error sources.

Concerning the SSM input, we take from [41] the central values for the fluxes ( $\Phi_{\text{pp}}, \Phi_{\text{pep}}, \Phi_{\text{Be}}, \Phi_{\text{B}}, \Phi_{\text{N}}, \Phi_{\text{O}}$ ), but re-

<sup>7</sup>The prescription in Eq. (14) is intermediate between the extreme possibilities of quadratic sum [21] and linear sum [34] over all flux components. We observe that this prescription is not only justified by the physics of the  $\nu_e$  absorption processes in Cl and Ga [33], but also by the effective separation of the Cl and the Ga solar  $\nu$  response functions into two “ $L$ ” and “ $H$ ” clusters in the energy domain [35,36].

<sup>8</sup>We conservatively assume the largest between the  $+1\sigma$  and  $-1\sigma$  asymmetric Ga cross section errors.

scale  $\Phi_{\text{hep}}$  from the value in [41] ( $9.3 \times 10^3 \text{ cm}^{-2} \text{ s}^{-1}$ ) to our default value

$$\Phi_{\text{hep}} = 8.3 \times 10^3 \text{ cm}^{-2} \text{ s}^{-1}, \quad (15)$$

according to the recent evaluation of the associated  $S_{\text{hep}}$  factor in [42].

The SSM also embeds a set of eleven sources  $X_k$  of correlated uncertainties (the cross section factors  $S_{11}, S_{13}, S_{34}, S_{1,14}, S_{17}$ , the Be capture cross section  $C_{\text{Be}}$ , the Sun luminosity, metallicity  $Z/X$ , age, opacity, and element diffusion), with fractional uncertainties  $\Delta \ln X_k$ , as listed in [37]. With respect to the compilation in [37], we update  $\Delta \ln Z/X = 0.061$  from [41], and we add  $X_{12} = S_{\text{hep}}$ , with  $\Delta \ln S_{\text{hep}} = 0.3$ .<sup>9</sup> The effects of such sources of uncertainties on the neutrino fluxes  $\Phi_i$  are characterized by log-derivatives [10,21],  $\alpha_{ik} = \partial \ln \Phi_i / \partial \ln X_k$ , as compiled in [37]. Concerning  $X_{12}$ , the only nonzero log-derivative is  $\alpha_{\text{hep},12} = 1$ .

The collective effect of the SSM sources of systematics  $X_k$  amounts to shift the neutrino fluxes as

$$\Phi_i \rightarrow \Phi_i \left( 1 + \sum_{k=1}^{12} \xi_k \alpha_{ik} \Delta \ln X_k \right), \quad (16)$$

where the  $\xi^k$ 's, penalized by the quadratic term  $\sum_{k=1}^{12} \xi_k^2$  in the expression of  $\chi_{\text{pull}}^2$ , are minimized away in the fit. Notice that the above equation is the linearized form of the power laws connecting each flux to the  $X_k$ 's [10,43]. Such linear form satisfies the luminosity constraint for the fluxes [44] by construction, due to the sum rule discussed in Refs. [21,37] (see also [45]).

Within the pull approach, the shifts in Eq. (16) are easily propagated to all theoretical predictions  $R_n^{\text{theor}}$ . In particular, if  $R_{n,i}^{\text{theor}}$  is the  $i$ -th flux contribution to  $R_n^{\text{theor}}$ , then the associated correlated shift from the  $k$ -th source is  $\xi_k c_{n,i}^k = \xi_k R_{n,i}^{\text{theor}} \alpha_{ik} \Delta \ln X_k$ . The net effect of the shifts in Eq. (16) is thus the generation of correlated errors on the  $R_n$ 's, which is strictly equivalent to the construction of the astrophysical error matrix defined in the earlier covariance approach [21,37], as also noticed in [24].

The 13th source of correlated systematics in our list is the  ${}^8\text{B}$   $\nu$  spectrum shape uncertainty [46] around the currently adopted “central” spectrum [47], which affects all the 81 observables<sup>10</sup> at the same time. In the absence of oscillations, we estimate that a  $+1\sigma$  perturbation of the  ${}^8\text{B}$   $\nu$  spectrum (in the direction of higher  $\nu$  energies) generates a  $+2.2\%$  and a  $+1.7\%$  increase of the  $\Phi_B$  component of the  $R_{\text{Ga}}$  and  $R_{\text{Cl}}$  theoretical rates, respectively (the evaluation is repeated in each point of the mass-mixing plane). The corresponding shifts for the SK and SNO spectra are evaluated in Appendix C and D, respectively. Notice that we conservatively use the

<sup>9</sup>The authors of [42] quote an uncertainty of  $\sim 15\%$  for  $S_{\text{hep}}$ , that we conservatively double to  $30\%$ .

<sup>10</sup>With the possible exception of the Ga winter-summer difference, where its effects cancel to a large extent, and can be safely neglected as compared with the rather large statistical error (see Appendix B).

TABLE I. Positions and values of the absolute minimum (LMA) and of three relevant local minima (LOW, QVO, SMA) of  $\chi^2_{\text{pull}}$ , together with the separate contributions from pulls of observables ( $\chi^2_{\text{obs}}$ ) and of correlated systematics ( $\chi^2_{\text{sys}}$ ). The corresponding  $\Delta\chi^2$  variations are also given.

Solution	$\delta m^2$ (eV <sup>2</sup> )	$\tan^2\theta_{12}$	$\chi^2_{\text{obs}}$	$\Delta\chi^2_{\text{obs}}$	$\chi^2_{\text{sys}}$	$\Delta\chi^2_{\text{sys}}$	$\chi^2_{\text{pull}}$	$\Delta\chi^2_{\text{pull}}$
LMA	$5.5 \times 10^{-5}$	0.42	71.3	—	2.1	—	73.4	—
LOW	$7.3 \times 10^{-8}$	0.67	79.7	8.4	4.1	2.0	83.8	10.4
QVO	$6.5 \times 10^{-10}$	1.33	74.9	3.6	6.3	4.2	81.2	7.8
SMA	$5.2 \times 10^{-6}$	$1.1 \times 10^{-3}$	83.1	11.8	13.8	11.7	96.9	23.5

<sup>8</sup>B  $\nu$  spectrum shape uncertainties estimated in [46] rather than the (smaller) ones estimated in [47] since, in our opinion, the issue of significant [ $O(100)$  keV] energy calibration differences among existing <sup>8</sup>B decay spectrum measurements [46,47] is not completely clarified, and warrants further experimental investigations.<sup>11</sup>

There are also eleven sources of correlated systematics, which affect only the SK spectrum. They include the SK energy scale and resolution uncertainties, an overall SK rate offset, and eight sources of systematics separately affecting the eight energy bins, with full correlation in nadir [6] (see Appendix C).

Finally, there are seven sources of correlated systematics, which affect only the SNO spectrum. They include: the uncertainties affecting the SNO energy scale and resolution, the event vertex reconstruction, the neutron capture efficiency, the neutron and low-energy (LE) background estimates and the interaction cross sections. See Appendix D for more details.

### C. Output

As output of the pull analysis, we get the function  $\chi^2_{\text{pull}}(\delta m^2, \tan^2\theta_{12})$  (essential to identify absolute and local minima and to draw confidence level contours), as well as other useful statistical indicators.

Concerning  $\chi^2_{\text{pull}}$ , for any *fixed* point in the parameter space ( $\delta m^2, \tan^2\theta_{12}$ ), the goodness-of-fit test requires  $\chi^2_{\text{pull}} \sim N$  ( $N=81$ ) for an acceptable fit. Further information can be gained by splitting  $\chi^2_{\text{pull}}$  into the separate contributions  $\chi^2_{\text{obs}}$  and  $\chi^2_{\text{sys}}$  [Eqs. (9) and (10)], obtained by summing up the squared pulls of the  $N=81$  observables [ $\bar{x}_n$ , see Eq. (8)] and of the  $K=31$  systematics [ $\bar{\xi}_k$ , see Eq. (A6)]. The larger the value of  $\chi^2_{\text{sys}}$ , the more the fit tends to “stretch” one or more correlated systematics to get a better agreement between data and expectations. Apart from global features, the analysis of the pull sets  $\{\bar{x}_n\}$  and  $\{\bar{\xi}_k\}$  allows to quantify individual contributions to the  $\chi^2$ , which, if anomalously large, might be indicative of problems either in the theoretical predictions or in the experimental measurements. Therefore, we think it useful to present, besides the global values of  $\chi^2_{\text{pull}} = \chi^2_{\text{obs}} + \chi^2_{\text{sys}}$ , also some selected lists of pulls.

<sup>11</sup>We have been informed that a new <sup>8</sup>B( $\beta^+$ )<sup>8</sup>Be( $2\alpha$ ) decay spectral measurement is in progress at Argonne [W. T. Winter (private communication)].

Finally, it is useful to isolate the twelve SSM systematic pulls  $\{\bar{\xi}_k\}_{k=1, \dots, 12}$  which, on the basis of Eq. (16), allow us to derive the induced neutrino flux shifts from the SSM central values, namely

$$\frac{\Delta\Phi_i}{\Phi_i} = \sum_{k=1}^{12} \bar{\xi}_k \alpha_{ik} \Delta \ln X_k. \quad (17)$$

These shifts provide valuable (and luminosity-constrained) information about the preferred departures from the SSM within the various oscillation solutions to the solar neutrino problem.

Summarizing, we will show and discuss results about pulls,

$$\{\bar{x}_n\}_{n=1, \dots, 81} = \text{pulls of the observables}, \quad (18)$$

$$\{\bar{\xi}_k\}_{k=1, \dots, 31} = \text{pulls of the correlated systematics}, \quad (19)$$

about  $\chi^2$  values,

$$\chi^2_{\text{obs}} = \sum_{n=1}^{81} \bar{x}_n^2, \quad (20)$$

$$\chi^2_{\text{sys}} = \sum_{k=1}^{31} \bar{\xi}_k^2, \quad (21)$$

$$\chi^2_{\text{pull}} = \chi^2_{\text{obs}} + \chi^2_{\text{sys}}, \quad (22)$$

and about fractional shifts from the SSM predictions,

$$\Delta\Phi_i/\Phi_i = \nu \text{ flux shifts}. \quad (23)$$

## IV. RESULTS OF THE $\chi^2_{\text{pull}}$ ANALYSIS

In this section we start by describing the global results of the  $\chi^2_{\text{pull}}$  analysis, and then we break down such results at increasing levels of detail.

### A. Global results

The global results of our solar  $\nu$  oscillation fit are summarized in Table I and in Fig. 1. In Table I we report the ( $\delta m^2, \tan^2\theta_{12}$ ) coordinates of the best-fit point [so-called large mixing angle (LMA) solution] and of the three deepest

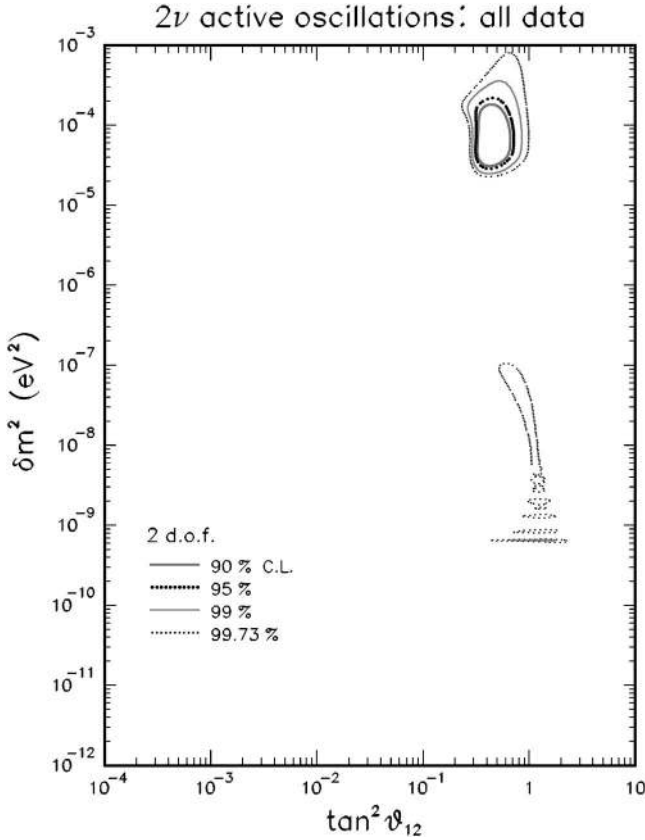


FIG. 1. Global results of the solar neutrino data analysis, including 81 observables and 31 sources of correlated systematics. The parameter space  $(\delta m^2, \tan^2 \theta_{12})$  refers to the scenario of  $2\nu$  oscillations among active states. The relevant  $\chi^2$  minima in the LMA, LOW, and QVO regions are given in Table I.

(local)  $\chi^2_{\text{pull}}$  minima in the regions of low  $\delta m^2$  (LOW), quasivacuum oscillations<sup>12</sup> (QVO), and small mixing angle (SMA).

Concerning the goodness-of-fit test, we recall that, at the absolute minimum, one expects the total  $\chi^2$  to be in the  $\pm 1\sigma$  range  $N_{\text{DF}} \pm \sqrt{2N_{\text{DF}}}$  [50]. In our case ( $N_{\text{DF}} = 81 - 2$ ), it is  $\chi^2_{\text{pull}} = 73.4$  at the LMA best-fit point, well within the expected range  $79 \pm 12.6$ . Also the LOW and especially the QVO solutions have acceptable values of  $\chi^2_{\text{pull}}$ , while the SMA value appears to be significantly larger than expected. The pull analysis will confirm that the LOW and QVO solutions are still viable, while the SMA solution is no longer statistically acceptable. Notice that at the LMA point, most of the contribution to  $\chi^2_{\text{pull}}$  comes from pulls of observables ( $\chi^2_{\text{obs}}$ ) rather than systematics ( $\chi^2_{\text{sys}}$ ). All the other solutions in Table I show an increase of both  $\chi^2_{\text{pull}}$  and  $\chi^2_{\text{sys}}$ , implying an increasing departure of the theoretical predictions from

<sup>12</sup>We do not find acceptable solutions in the octant-symmetric vacuum oscillation (VO) regime. For the QVO solution in Table I, only the highest energy  $\nu$  flux components ( $\Phi_B$  and  $\Phi_{\text{hep}}$ ) have reached the VO regime, while the lowest energy ones are still affected by octant-asymmetric quasivacuum effects [48,49] in the Sun.

the data and of the systematics offsets from zero.

Concerning the parameter estimation test<sup>13</sup> (based on  $\Delta\chi^2_{\text{pull}}$  variations around the minimum) Fig. 1 shows the results of our global analysis in the usual mass-mixing plane. The confidence level isolines are drawn at  $\Delta\chi^2 = 4.61, 5.99, 9.21,$  and  $11.83$ , corresponding to 90%, 95%, 99%, and 99.73% joint probability regions for the two  $(\delta m^2, \tan^2 \theta_{12})$  parameters. The QVO and LOW parameters are still acceptable at the 99% and 99.73% C.L., respectively, while the SMA parameters are basically ruled out. Our LMA bounds appear to be (sometimes significantly) more conservative than in other recent analyses [6,9,15–20].<sup>14</sup> In particular, at the 99.73% C.L. we derive from Fig. 1 that: (i) maximal mixing is marginally allowed in the LMA region, and (ii) the highest  $\delta m^2$  allowed values hit the region independently disfavored by CHOOZ data [53].<sup>15</sup> We think that the detailed treatment of all known uncertainties (and of their propagation to all relevant experimental observables) plays a role in such different results, also for non-LMA solutions. Concerning the LOW solution, we note that the inclusion of the winter-summer datum from GALLEX-GNO contributes to decrease its likelihood in our analysis.

## B. Separating experimental bounds

Figure 2 show the decomposition of the global results into contributions from the Cl experiment (total rate), from the Gallium experiments (total rate and winter-summer difference), from the SK energy-nadir spectrum (44 bins), and from the SNO day-night spectrum (34 bins). In each panel, the results are shown in terms of allowed regions, for the same confidence levels as in Fig. 1 (referred to the absolute minimum in each panel).

Concerning the  $\chi^2_{\text{pull}}$  minima in Fig. 2, their positions are not particularly interesting for the Cl and Ga cases, where they are essentially degenerate. More interesting is the case of the SK experiment alone, where the best fit ( $\chi^2_{\text{pull}} = 38.4$ ) is reached at maximal mixing and for  $\delta m^2 = 6.5 \times 10^{-10}$  eV<sup>2</sup> (in agreement with the results in [54]), very close to the QVO coordinates in Table I. Concerning the fit to SNO data only, we find the best fit at  $\delta m^2 = 3.7 \times 10^{-5}$  eV<sup>2</sup> and  $\tan^2 \theta_{12} = 0.47$ , close to the LMA coordinates in Table I, with  $\chi^2_{\text{pull}} = 25.7$ . The latter value appears to be on the lower side of the  $\pm 1\sigma$  expected range for the  $\chi^2_{\text{pull}}$  in SNO ( $32 \pm \sqrt{64}$ ).<sup>16</sup>

<sup>13</sup>Useful discussions of the applications and differences between the goodness-of-fit test and the parameter estimation test can be found in [50–52].

<sup>14</sup>The closest agreement is reached with the global allowed LMA region in Ref. [18].

<sup>15</sup>CHOOZ data are not included in the present analysis, in order to show more clearly the strength of the upper bound on  $\delta m^2$  placed by solar neutrino data alone.

<sup>16</sup>We think that this feature might be partly due to nonoptimal binning of the SNO spectrum. Although, at low energy, relatively dense binning is required to enhance the effects of the neutral current component, at high energies it is preferable to enlarge the bin

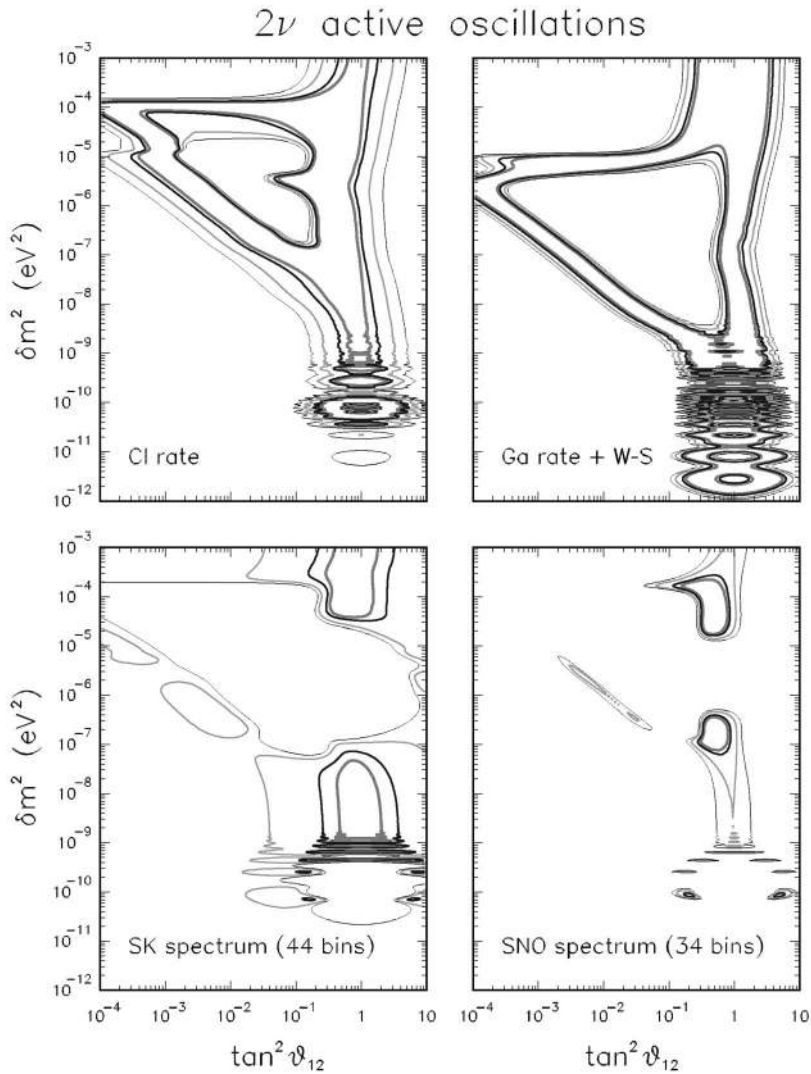


FIG. 2. Results of the solar neutrino data analysis, as obtained by separating four classes of observables: (i) the chlorine rate; (ii) the average SAGE+GALLEX-GNO gallium rate plus the GALLEX-GNO winter-summer difference; (iii) the SK energy-nadir spectrum; and (iv) the SNO day-night spectrum.

Concerning the shapes of the allowed regions in Fig. 2, we note the following facts. None of the experiments excludes maximal mixing and  $\delta m^2 \rightarrow \infty$  at 99% C.L. This feature is rather well known for Ga and SK data, but does not appear in all recent analyses for the Cl and SNO data. For instance, the Cl contours in Ref. [6] appear to be more restrictive than ours, which might be due to different estimates of the Cl errors. We also note some differences between our SNO bounds in Fig. 2 and the SNO official analysis in Fig. 4(a) of [9]: (a) in the QVO region, our contours are smooth (as they should); (b) we do not find (Q)VO solutions at maximal mixing for  $\delta m^2 \sim 10^{-10}$  eV<sup>2</sup>; (c) our bounds in the LMA region allow maximal mixing and  $\delta m^2 \rightarrow \infty$  well within the 99.73% C.L. Concerning the points (a) and (b), we think that the differences might depend in [9] on the (numerically delicate) averaging of the oscillating terms in the energy or time domain. Concerning the points (b) and (c), some differences might also be due to the fact that the analysis in Fig. 4(a) of [9] is done without SSM input. Concerning the point (c), we

width so as to match the SNO energy resolution width (analogously to the current SK energy spectrum binning).

note that the exclusion of  $\delta m^2 \rightarrow \infty$  and of  $\tan^2 \theta_{12} = 1$  at the 99.73% level by the SNO data alone (as found in Fig. 4(a) of [9]) would be equivalent to the exclusion of the constant  $P_{ee} = 1/2$  case (or of equal  $\nu_e$  and  $\nu_{\mu,\tau}$  fluxes,  $\Phi_e = \Phi_{\mu,\tau}$ ) at the same confidence level. Although the SNO data clearly prefer  $P_{ee} \sim 1/3$  [8] (see also Appendix E), a  $3\sigma$  rejection of  $P_{ee} \approx 1/2$  might be premature. Indeed, from Fig. 3 of [8] it appears that the  $\Phi_e = \Phi_{\mu,\tau}$  line touches the 95% error ellipse determined by the total SNO rates. Given that the exclusion of relatively large values of  $\delta m^2$  and  $\tan^2 \theta$  has profound implications in lepton physics (both phenomenologically and theoretically), we think that the impact of the SNO data on such values warrants further investigations.

From Fig. 2 it also appears that all experiments largely agree in the LMA region, and that a few QVO “islands” below  $10^{-9}$  eV<sup>2</sup> also happen to be consistent with all experiments. Moreover, all the experiments appear to be generically consistent with some “LOW” or “SMA” regions at least at 99% C.L. However, such regions are somewhat different for the different panels in Fig. 2. Concerning the LOW case, there is a reasonable overlap of the Cl, Ga, and SK bounds at  $\delta m^2 \lesssim 10^{-7}$  eV<sup>2</sup>, while SNO prefers  $\delta m^2$

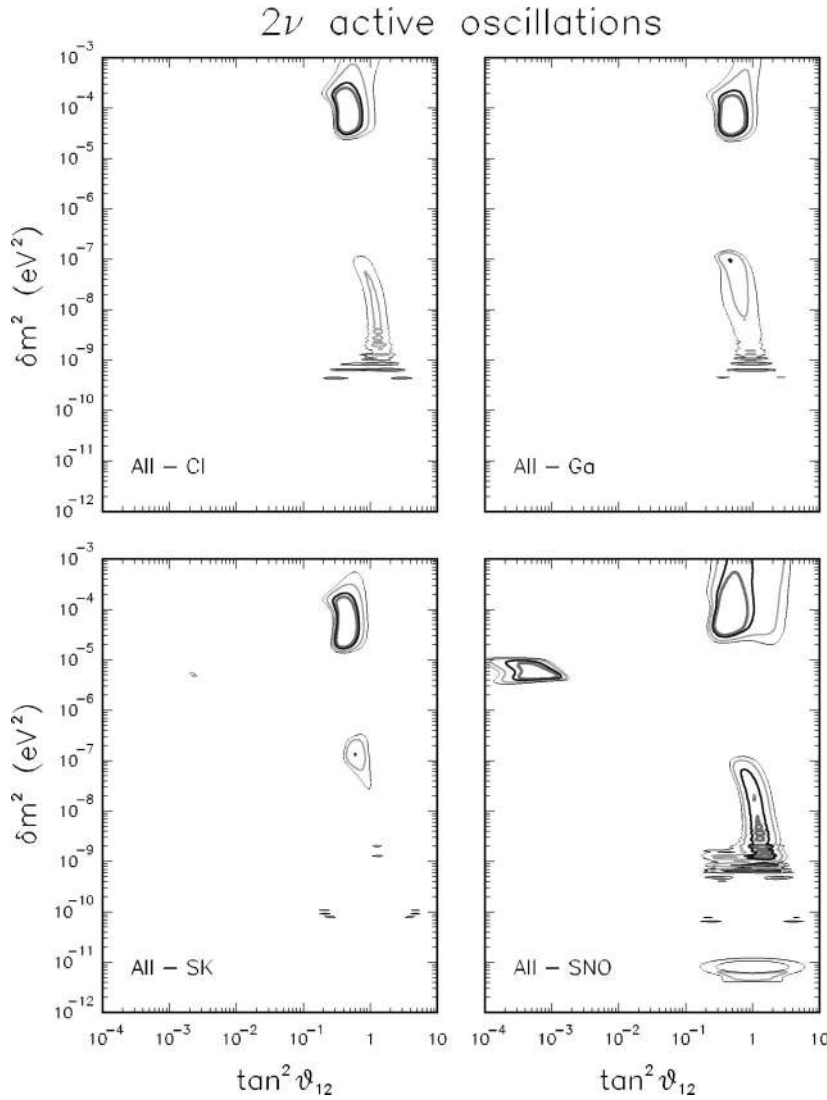


FIG. 3. Results of the solar neutrino data analysis, as obtained by excluding each of the four data sets in Fig. 2 from the global set used in Fig. 1.

$\gtrsim 10^{-7}$  eV<sup>2</sup>, where the LOW parameters more easily adapt to the preferred value  $P_{ee} \approx 1/3$ . This tension generates an overall decrease of the LOW likelihood. Concerning the SMA case, the low- $\tan^2 \theta_{12}$  regions separately allowed by Cl, Ga, SK, and SNO at the 99.73% C.L. do not overlap.

Figure 3 allows to appreciate the impact of each experiment in the global fit, by removing one experiment at a time. In a sense, Fig. 3 is the “difference” between Fig. 1 and Fig. 2. It can be seen that the removal of either the Cl or the Ga experiments (upper panels in Fig. 3) weakens the bounds on large mixing, on large values of  $\delta m^2$ , and on the LOW parameters, but does not alter the situation for vacuum oscillations, which are excluded in both cases.<sup>17</sup> The lower left panel in Fig. 3 shows that the removal of the SK experiment

would diminish the likelihood of the solutions characterized by no or mild energy spectrum distortion (e.g.,  $\delta m^2 \rightarrow \infty$  or QVO cases), and, conversely, would make some strongly energy-dependent solutions marginally reappear (at small mixing and in the vacuum regime). Finally, the lower right panel in Fig. 3 shows the pre-SNO situation (but with updated SK, Cl, and Ga data), with all the well-known multiple solutions to the solar neutrino problem.

The comparison of Figs. 1–3 shows the dramatic impact of SK and SNO in determining the preference for large mixing (and especially for the LMA solutions) and the rejection of the SMA solution. However, the Cl and Ga data still play an important role in determining the shape of the LMA contours, as well as the likelihood of the less favored solutions (LOW and QVO), which cannot be rejected on the basis of the present global information.

### C. Separating and grouping pulls

We discuss the decomposition of  $\chi_{\text{pull}}^2$  into separate and grouped pulls of observables  $\{\bar{x}_n\}$  and of correlated systematics  $\{\bar{\xi}_k\}$  [see Eqs. (18)–(22)] for the various solutions.

<sup>17</sup>In Ref. [20], the Ga impact on the LOW solution has been studied by lowering the total rate from  $70.8 \pm 4.4$  to  $66.1 \pm 5.3$  SNU. The authors of [20] find a corresponding reduction of the  $\Delta\chi_{\text{LOW}}^2$  from 6.9 to 3.0, with respect to the LMA minimum. By repeating the same exercise, we find a smaller effect: our  $\Delta\chi_{\text{LOW}}^2$  decreases from 10.4 (see Table I) to 9.0.



Table II shows the pulls of each of the 81 observables used in our analysis, corresponding to the four solutions in Table I.<sup>18</sup> For the best-fit LMA solution, we also give the range spanned by each pull within the 99.73% C.L. LMA region shown in Fig. 1. It can be seen that, in any case, there are no anomalously large (say,  $>3$  standard deviation) pulls—not even in the SMA solution or at the borders of the LMA region. This fact confirms the results of the previous sections, namely, that the allowance or rejection of the various solutions comes from a “collective” effect of several experimental observables rather than by a small subset of them.

Figure 4 provides a graphical version of the first three columns in Table II, together with an histogram of the pull distribution, compared with a Gaussian distribution (conventionally normalized to  $N=81$ ) to guide the eye. It appears that the pulls of the observables have a reasonably symmetrical and Gaussian distribution, confirming the goodness of the LMA fit at a deeper level than the global  $\chi^2$  values. The relatively large pull for the CI datum ( $-1.74$ ) may be regarded as a statistical fluctuation among the others, at the LMA best fit. Notice that the CI pull in the SMA solution is instead very small (0.14). Retrospectively, this small pull, together with theoretical prejudices against large mixing, appears to be at the origin of a very long detour towards small-mixing oscillations in matter. The distributions of pulls of the observables for the QVO and LOW cases (not graphically shown) are also reasonably Gaussian as for the LMA case, although with a slightly larger area (given by the corresponding  $\chi_{\text{obs}}^2$  values in Table I). The distribution of pulls for the SMA case (not shown), besides having an even larger area ( $\chi_{\text{obs}}^2=83.1$ ), appears also to be slightly skewed, with an excess of positive pulls. This adds to the statistical problems of this solution.

It is interesting to group the separate experimental contributions to the global  $\chi_{\text{obs}}^2$  in Table I, by summing up the corresponding squared pulls from Table II. The results of this exercise, as reported in Table III, show which experiment “wins” or “loses” in the various global solutions. In particular, the radiochemical experiments clearly win in the SMA and loose in the QVO and LOW solutions, while the fit to the SK spectrum observables appears to be rather stable, with only  $\Delta\chi_{\text{obs}}^2 \approx \pm 3$  variations in the various solutions. The SMA solution tries to make a compromise between SK and SNO data, in which SK dominates (having smaller spectral errors), leaving SNO with a worse fit ( $\chi_{\text{obs}}^2=38.5$ ) as compared with the LMA case ( $\chi_{\text{obs}}^2=26.2$ ).

Let us now consider the contributions of correlated systematics shifts to the global fit. Table IV shows the contributions of the pulls of systematics in the various solutions. As in Table II, for the LMA solution we also show the range spanned by the pulls within the 99.73% C.L. LMA region in Fig. 1. It appears that such pulls are generally rather small,

and typically assume minimal values in the LMA solution. In particular, Fig. 5 shows the LMA pull diagram for the correlated systematics, none of which presents a significant offset. The smallness of all SSM input offsets (with the possible exception of  $S_{17}$ ) is particularly impressive. In general, at the LMA best-fit point there is no need to stretch any correlated systematics to fit the data. In the LOW and QVO solutions the situation is less ideal (several offsets in Table IV are at the level of  $\sim 0.5\sigma$ ) but certainly still acceptable. In the SMA case, however, several SNO systematic offsets in Table IV are at the level of  $\sim 1\sigma$ , and the  ${}^8\text{B}$   $\nu$  shape uncertainty is stretched by  $\sim 1.5\sigma$ . Such offsets, which act in the direction of reducing the spectral differences between theory and data, produce a significant contribution to the SMA fit ( $\chi_{\text{sys}}^2=13.8$ ). It is quite unlikely that future, possible recalibrations of systematics may just happen to cancel out all these offsets, thus giving more chances to the SMA solution.

It is interesting to group some  $\chi^2$  contributions of systematics, according to their origin. This exercise is done in Table V. The SK contribution to  $\chi_{\text{sys}}^2$  is rather stable (and small), with a minimum at the QVO solution. This situation parallels the SK contribution to  $\chi_{\text{obs}}^2$  (see Table III and related comments), and show the pivoting role of the SK spectrum in determining the likelihood of all solutions. Conversely, the contributions to  $\chi_{\text{sys}}^2$  from SNO and from the standard neutrino flux input (SSM and  ${}^8\text{B}$   $\nu$  shape systematics) increase significantly when passing from the LMA to the SMA solution.

The grand total of the various contributions to the  $\chi_{\text{pull}}^2$  from both observables and systematics is shown in Table VI. This table shows quantitatively that the LMA solution is in very good agreement with both the experimental data and with the SSM. The LOW and QVO solutions provide a slightly less good agreement with the SSM and with SK+SNO, and are somehow “borderline” from the point of view of radiochemical experiments. However, they cannot be really excluded by any data at present. The SMA solution is instead safely ruled out, mainly as a consequence of the SNO data fit ( $\chi_{\text{SNO}}^2=45.1$ ).

#### D. Implications for the SSM neutrino fluxes

In the previous section, we have seen that the LMA solution does not require any significant offset  $\bar{\xi}_k$  in the SSM input systematics ( $k=1, \dots, 12$ ), and that such offsets are relatively small also in the other solutions. Equation (17) allows to translate such offsets into preferred shift of the neutrino fluxes  $\Phi_i$  from their SSM central values. The results are shown in Table VII for the various solutions. In the LMA best-fit point, all solar neutrino fluxes are basically confirmed: just for illustration, an approximate translation of the LMA flux shifts into variations of the “effective solar core temperature” ( $\Delta t_c/t_c$  [37,43,45]) would formally provide  $|\Delta t_c/t_c| \leq 0.2\%$ . The QVO and SMA solutions would formally require  $-\Delta t_c/t_c \sim 0.5\text{--}1\%$  (a slightly cooler Sun), the LOW case being intermediate between the latter and the LMA one. In all solutions, the preferred  $\Phi_{\text{pp}}$  values are within a percent from the SSM. The preferred (negative)

<sup>18</sup>The SK and SNO spectrum bins are identified by their energy range and by their nadir interval (day and night bins). See also Appendixes C and D for notation.

TABLE II. Pulls of the observables in the various solutions.

$n$	Observable	LMA	LMA [min, max] at $3\sigma$	LOW	QVO	SMA
1	Cl rate	-1.74	[-2.56, -1.17]	-1.86	-2.68	0.14
2	Ga rate	0.39	[-1.49, +1.90]	1.27	0.84	-0.19
3	Ga $W-S$	-1.23	[-1.23, -1.22]	-1.75	-1.25	-1.22
4	SK [5.0,5.5]	-0.09	[-0.46, +0.10]	0.14	-0.01	0.58
5	SK [5.5,6.5] day	-0.36	[-1.06, +0.40]	-0.06	-0.52	0.17
6	SK [5.5,6.5] M1	-0.41	[-0.63, -0.29]	-0.27	-0.40	-0.14
7	SK [5.5,6.5] M2	-1.77	[-2.00, -1.64]	-1.84	-1.72	-1.43
8	SK [5.5,6.5] M3	0.03	[-0.20, +0.26]	0.05	0.19	0.52
9	SK [5.5,6.5] M4	1.11	[+0.93, +1.36]	1.46	1.30	1.64
10	SK [5.5,6.5] M5	0.62	[+0.47, +0.86]	0.71	0.80	1.14
11	SK [5.5,6.5] core	-0.90	[-1.04, -0.67]	-0.75	-0.73	-0.41
12	SK [6.5,8.0] day	1.20	[+0.48, +2.35]	1.15	0.56	0.72
13	SK [6.5,8.0] M1	1.97	[+1.80, +2.04]	1.99	1.84	1.90
14	SK [6.5,8.0] M2	1.31	[+0.82, +1.38]	1.08	1.29	1.37
15	SK [6.5,8.0] M3	-1.29	[-1.80, -1.07]	-1.39	-1.13	-1.02
16	SK [6.5,8.0] M4	0.19	[-0.23, +0.46]	0.62	0.41	0.55
17	SK [6.5,8.0] M5	-0.81	[-1.17, -0.54]	-0.78	-0.60	-0.40
18	SK [6.5,8.0] core	-1.12	[-1.41, -0.87]	-0.99	-0.94	-0.73
19	SK [8.0,9.5] day	-0.40	[-0.93, +0.56]	-0.67	-0.91	-1.29
20	SK [8.0,9.5] M1	0.17	[+0.05, +0.19]	0.13	0.09	-0.05
21	SK [8.0,9.5] M2	0.24	[-0.32, +0.42]	0.06	0.31	0.17
22	SK [8.0,9.5] M3	-0.17	[-0.73, +0.15]	-0.22	0.08	-0.05
23	SK [8.0,9.5] M4	1.40	[+0.92, +1.76]	1.75	1.70	1.61
24	SK [8.0,9.5] M5	-0.26	[-0.65, +0.09]	-0.20	0.02	0.03
25	SK [8.0,9.5] core	-0.51	[-0.83, -0.21]	-0.39	-0.28	-0.23
26	SK [9.5,11.5] day	-0.67	[-1.19, +0.19]	-1.07	-0.83	-1.70
27	SK [9.5,11.5] M1	-0.20	[-0.36, -0.13]	-0.29	-0.17	-0.49
28	SK [9.5,11.5] M2	1.01	[+0.45, +1.30]	0.88	1.22	0.90
29	SK [9.5,11.5] M3	-0.55	[-1.11, -0.10]	-0.56	-0.13	-0.49
30	SK [9.5,11.5] M4	0.08	[-0.43, +0.57]	0.40	0.55	0.26
31	SK [9.5,11.5] M5	0.17	[-0.21, +0.63]	0.26	0.57	0.45
32	SK [9.5,11.5] core	0.33	[+0.01, +0.69]	0.43	0.62	0.52
33	SK [11.5,13.5] day	0.72	[+0.36, +1.31]	0.42	0.66	0.11
34	SK [11.5,13.5] M1	0.67	[+0.57, +0.71]	0.61	0.71	0.52
35	SK [11.5,13.5] M2	-2.21	[-2.64, -1.98]	-2.25	-2.00	-2.23
36	SK [11.5,13.5] M3	-1.76	[-2.11, -1.43]	-1.72	-1.39	-1.65
37	SK [11.5,13.5] M4	0.36	[+0.02, +0.69]	0.57	0.70	0.55
38	SK [11.5,13.5] M5	-0.80	[-1.02, -0.50]	-0.72	-0.59	-0.54
39	SK [11.5,13.5] core	0.67	[+0.46, +0.92]	0.76	0.76	0.82
40	SK [13.5,16.0] day	0.65	[+0.36, +1.02]	0.50	-0.37	0.48
41	SK [13.5,16.0] M1	0.59	[+0.52, +0.61]	0.56	0.25	0.57
42	SK [13.5,16.0] M2	2.03	[+1.88, +2.06]	2.03	1.79	2.08
43	SK [13.5,16.0] M3	1.51	[+1.39, +1.57]	1.54	1.26	1.62
44	SK [13.5,16.0] M4	1.31	[+1.18, +1.39]	1.42	1.05	1.47
45	SK [13.5,16.0] M5	-0.48	[-0.57, -0.41]	-0.42	-0.85	-0.26
46	SK [13.5,16.0] core	-0.22	[-0.30, -0.15]	-0.15	-0.60	-0.08
47	SK [16.0,20.0]	0.34	[+0.06, +0.47]	0.31	-0.19	0.35
48	SNO [5.0,5.5] day	-0.99	[-1.32, -0.28]	-0.49	-0.66	-0.08
49	SNO [5.0,5.5] night	0.23	[-0.17, +1.01]	0.78	0.65	1.19
50	SNO [5.5,6.0] day	0.94	[+0.63, +1.42]	1.23	1.06	1.33
51	SNO [5.5,6.0] night	-0.31	[-0.65, +0.12]	-0.36	-0.64	-0.60
52	SNO [6.0,6.5] day	0.09	[-0.53, +0.64]	-0.26	-0.60	-0.74
53	SNO [6.0,6.5] night	-0.72	[-1.55, -0.02]	-1.27	-1.52	-1.88

TABLE II. (*Continued*).

$n$	Observable	LMA	LMA [min, max] at $3\sigma$	LOW	QVO	SMA
54	SNO [6.5,7.0] day	-0.64	[-1.46, +0.10]	-1.24	-1.20	-1.82
55	SNO [6.5,7.0] night	1.34	[+0.70, +1.95]	0.84	1.17	0.40
56	SNO [7.0,7.5] day	-0.66	[-1.24, -0.05]	-1.14	-0.57	-1.51
57	SNO [7.0,7.5] night	0.27	[-0.13, +0.74]	-0.09	0.38	-0.31
58	SNO [7.5,8.0] day	0.41	[+0.15, +0.79]	0.16	0.37	0.06
59	SNO [7.5,8.0] night	0.39	[+0.25, +0.68]	0.24	0.13	0.22
60	SNO [8.0,8.5] day	-0.20	[-0.26, +0.04]	-0.27	-0.65	-0.21
61	SNO [8.0,8.5] night	-0.69	[-0.73, -0.47]	-0.68	-1.20	-0.58
62	SNO [8.5,9.0] day	-1.31	[-1.39, -1.07]	-1.25	-1.78	-1.10
63	SNO [8.5,9.0] night	0.43	[+0.35, +0.60]	0.51	0.27	0.60
64	SNO [9.0,9.5] day	-0.72	[-0.96, -0.39]	-0.51	-0.20	-0.44
65	SNO [9.0,9.5] night	0.54	[+0.07, +1.35]	1.03	1.09	1.71
66	SNO [9.5,10.0] day	-0.95	[-1.59, +0.07]	-0.29	-0.19	0.50
67	SNO [9.5,10.0] night	-0.66	[-1.13, -0.07]	-0.27	-0.21	0.17
68	SNO [10.0,10.5] day	0.76	[+0.44, +0.85]	0.80	0.75	0.84
69	SNO [10.0,10.5] night	2.19	[+1.70, +2.43]	1.96	1.84	1.75
70	SNO [10.5,11.0] day	0.60	[-0.09, +1.02]	0.20	0.18	-0.14
71	SNO [10.5,11.0] night	-1.76	[-2.54, -1.22]	-2.24	-1.93	-2.60
72	SNO [11.0,11.5] day	0.78	[+0.15, +1.24]	0.41	0.99	0.17
73	SNO [11.0,11.5] night	-0.69	[-1.25, -0.21]	-0.98	-0.21	-1.13
74	SNO [11.5,12.0] day	0.27	[-0.17, +0.69]	0.10	0.69	0.08
75	SNO [11.5,12.0] night	-0.27	[-0.64, +0.10]	-0.33	-0.08	-0.25
76	SNO [12.0,12.5] day	1.28	[+1.01, +1.54]	1.31	1.17	1.45
77	SNO [12.0,12.5] night	0.89	[+0.66, +1.14]	1.00	0.59	1.19
78	SNO [12.5,13.0] day	-0.45	[-0.69, -0.13]	-0.26	-0.84	-0.03
79	SNO [12.5,13.0] night	0.64	[+0.44, +0.92]	0.82	0.40	1.02
80	SNO [13.0,20.0] day	1.37	[+1.21, +1.60]	1.54	1.33	1.68
81	SNO [13.0,20.0] night	-1.03	[-1.41, -0.57]	-0.64	-0.19	-0.51

variations of the  $\Phi_B$  values from its SSM value are instead significant in non-LMA solutions, and appear to be consistent with those derived in some  $\Phi_B$ -free analyses [18,19,54]. This might seem surprising, since we do not exclude any SSM input in our analysis. The reason for such agreement is that the current SNO data implicitly provide an experimental determination of  $\Phi_B$  which is already significantly more accurate than the SSM estimate; therefore, there is little difference in making the analysis with or without SSM input for  $\Phi_B$ . Notice that, in addition, we can also quantify the preferred variations of  $\Phi_{Be}$ ,  $\Phi_N$ , and  $\Phi_O$ , which appear to be all negative in non-LMA solutions.<sup>19</sup> Concerning  $\Phi_{hep}$ , we do not find any significant preferred variation with respect to Eq. (15). This fact is mainly due to the poor sensitivity of the data to this flux (confined to the last few bins in the SK and SNO spectrum) and possibly to our careful treatment of SK and SNO spectral uncertainties (see Appendixes C and D).

Finally, Fig. 6 shows isolines of the preferred neutrino flux shifts within the LMA solution (superposed at 99% C.L.). The variations of  $\Phi_{pp}$  and of  $\Phi_{pep}$  are limited to about a percent, but can be an order of magnitude larger for the

other neutrino fluxes. In the upper or right part of the LMA region, the current global fits seem to prefer variations of the fluxes roughly corresponding to a slightly “cooler” Sun, while in the lower left corner of the LMA region the trend is opposite (slightly “hotter” Sun). Should the best-fit LMA value be confirmed by the KamLand experiment [13], the current SSM input would be just “perfect.”

## V. SUMMARY AND CONCLUSIONS

We have performed a global analysis of solar neutrino oscillations within the  $2\nu$  active scenario,<sup>20</sup> including all the current solar neutrino data and all relevant sources of uncertainties. The statistical analysis has been performed in a way which clearly traces the residual contribution of each observable and of each source of correlated systematics in the  $\chi^2$  fit (“pull” method). It turns out that there is still a multiplicity of acceptable solutions at large mixing in the so-called LMA, LOW, and QVO regions (Fig. 1 and Table I), none of which contradict any data (Figs. 2 and 3), as also confirmed by a detailed pull analysis (Tables II–VI). In particular, the best-fit LMA solution appears to be in very good agreement with

<sup>19</sup>This information is relevant for prospective studies in the BOREXINO experiment [14].

<sup>20</sup>Three-flavor results will be shown elsewhere.

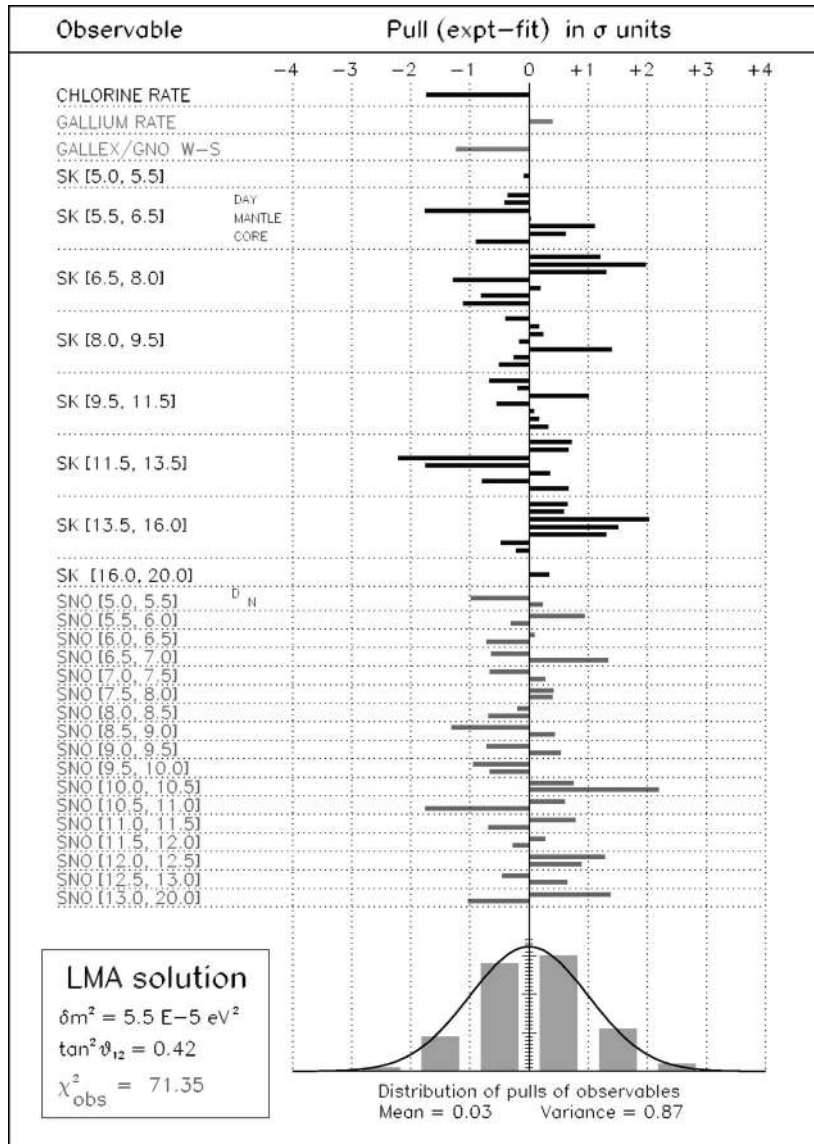


FIG. 4. Diagram of pulls  $\{\bar{x}_n\}_{n=1, \dots, 81}$  for observables at the LMA best-fit point. See the text for details.

all the data (Fig. 4), without requiring any stretching of the correlated systematics (Fig. 5), contrary to the strongly disfavored solution at small mixing angle. The striking LMA agreement with all standard solar model fluxes (Table VII) is only slightly worsened when moving away from the best fit (Fig. 6). The statistical techniques and the treatment of the data underlying these results have been discussed in detail in the Appendixes.

TABLE III. Separate experimental contributions to the global  $\chi^2_{\text{obs}}$  for the various solutions reported in Table I, as obtained by grouping squared pulls from Table II.

$n$	Experiment	LMA	LOW	QVO	SMA
1	Cl (rate)	3.0	3.4	7.2	0.0
2-3	Ga (rate and W-S)	1.7	4.7	2.3	1.5
4-48	SK (44 bins)	40.4	42.9	37.0	43.1
49-81	SNO (34 bins)	26.2	28.7	28.4	38.5
1-81	All (global $\chi^2_{\text{obs}}$ )	71.3	79.7	74.9	83.1

*Note added.* After completion of this work, the SAGE Collaboration has added the winter-summer difference datum in Ref. [2]. We thank B. Cleveland for related communications.

ACKNOWLEDGMENTS

We thank the organizers of the 20th International Conference on Neutrino Physics and Astrophysics in Munich—where preliminary results of this work were presented—for kind hospitality. We also thank the many participants to this Conference who have contributed useful comments, remarks, and suggestions. This work was supported in part by INFN and in part by the Italian *Ministero dell’Istruzione, Università e Ricerca* through the “Astroparticle Physics” research project.

APPENDIX A: PROOF OF  $\chi^2_{\text{covar}} = \chi^2_{\text{pull}}$

Let us recall that basic ingredients of any  $\chi^2$  statistics are: the experimental and theoretical values ( $R_n^{\text{expt}}$  and  $R_n^{\text{theor}}$ ) of

TABLE IV. Pulls of the systematics in the various solutions.

$k$	Systematic	LMA	LMA [min, max] at $3\sigma$	LOW	QVO	SMA
1	$S_{11}$	-0.05	[-0.31, +0.42]	0.19	0.35	0.34
2	$S_{33}$	0.00	[-0.13, +0.32]	0.10	0.24	0.18
3	$S_{34}$	0.01	[-0.98, +0.42]	-0.32	-0.72	-0.59
4	$S_{1,14}$	-0.15	[-0.49, -0.02]	-0.08	-0.21	-0.01
5	$S_{17}$	0.38	[-0.71, +1.15]	-0.35	-0.47	-0.83
6	Luminosity	0.04	[-0.31, +0.17]	-0.08	-0.20	-0.22
7	Z/X	0.03	[-0.89, +0.48]	-0.35	-0.68	-0.60
8	Age	0.00	[-0.06, +0.04]	-0.02	-0.05	-0.04
9	Opacity	-0.05	[-0.36, +0.52]	0.22	0.42	0.41
10	Diffusion	-0.02	[-0.26, +0.43]	0.18	0.34	0.31
11	$C_{\text{Be}}$	-0.07	[-0.22, +0.13]	0.07	0.09	0.16
12	$S_{\text{hep}}$	-0.03	[-0.04, +0.00]	-0.02	-0.10	0.02
13	$^8\text{B } \nu$ shape	0.17	[-0.71, +1.24]	-0.66	-0.80	-1.56
14	SK scale	0.78	[+0.51, +1.82]	0.49	0.49	-0.31
15	SK resolution	0.61	[+0.54, +0.87]	0.61	0.06	0.73
16	SK offset	0.44	[+0.33, +0.70]	0.57	0.68	0.34
17	SK [5.0,5.5]	-0.03	[-0.18, +0.05]	0.06	0.00	0.27
18	SK [5.5,6.5]	-0.26	[-0.61, -0.13]	-0.10	-0.28	0.34
19	SK [6.5,8.0]	0.54	[+0.32, +0.67]	0.70	0.52	0.89
20	SK [8.0,9.5]	0.01	[-0.06, +0.19]	-0.08	-0.03	-0.42
21	SK [9.5,11.5]	-0.14	[-0.25, +0.21]	-0.30	0.14	-0.76
22	SK [11.5,13.5]	-0.21	[-0.31, -0.06]	-0.29	-0.10	-0.45
23	SK [13.5,16.0]	0.26	[+0.23, +0.34]	0.32	0.11	0.44
24	SK [16.0,20.0]	0.01	[+0.00, +0.02]	0.02	-0.01	0.02
25	SNO scale	-0.15	[-0.90, +0.58]	-0.86	-1.49	-1.48
26	SNO resolution	-0.32	[-0.41, -0.05]	-0.16	-0.52	0.47
27	SNO vertex	0.13	[-0.60, +0.65]	-0.52	-0.20	-1.42
28	SNO $n$ capture	-0.10	[-0.46, +0.60]	0.42	0.34	0.94
29	SNO $n$ background	-0.06	[-0.27, +0.35]	0.25	0.20	0.55
30	SNO LE background	-0.16	[-0.49, +0.53]	0.33	0.28	0.87
31	SNO cross section	0.04	[-0.16, +0.21]	-0.16	-0.02	-0.52

the  $N$  observables to be fitted; the associated uncorrelated errors  $u_n$ ; and the associated set of fully correlated errors  $c_n^k$ , due to  $K$  independent sources of systematics ( $k = 1, \dots, K$ ).

In order to simplify the notation, we normalize both the differences  $R_n^{\text{expt}} - R_n^{\text{theor}}$  and the correlated errors  $c_n^k$  to the  $u_n$ 's, by defining

$$\Delta_n = \frac{R_n^{\text{expt}} - R_n^{\text{theor}}}{u_n}, \quad (\text{A1})$$

and

$$q_n^k = \frac{c_n^k}{u_n}. \quad (\text{A2})$$

Equation (5) reads then

$$\chi_{\text{covar}}^2 = \sum_{n,m=1}^N \Delta_n \left[ \delta_{nm} + \sum_k q_n^k q_m^k \right]^{-1} \Delta_m, \quad (\text{A3})$$

while Eq. (7) reads

$$\chi_{\text{pull}}^2 = \min_{\{\xi_k\}} \left[ \sum_{n=1}^N \left( \Delta_n - \sum_k q_n^k \xi_k \right)^2 + \sum_{k=1}^K \xi_k^2 \right], \quad (\text{A4})$$

where the  $\xi_k$  are Gaussian random variables with  $\langle \xi_k \rangle = 0$  and  $\langle \xi_k^2 \rangle = 1$ .

The minimization in Eq. (A4) leads to a set of  $K$  linear equations in the unknowns  $\bar{\xi}_k$ ,

$$\sum_{h=1}^K \left( \delta_{kh} + \sum_n q_n^k q_n^h \right) \bar{\xi}_h = \sum_{n=1}^N \Delta_n q_n^k, \quad (\text{A5})$$

whose solution is

$$\bar{\xi}_k = \sum_{h=1}^K S_{kh} \sum_{n=1}^N \Delta_n q_n^h, \quad (\text{A6})$$

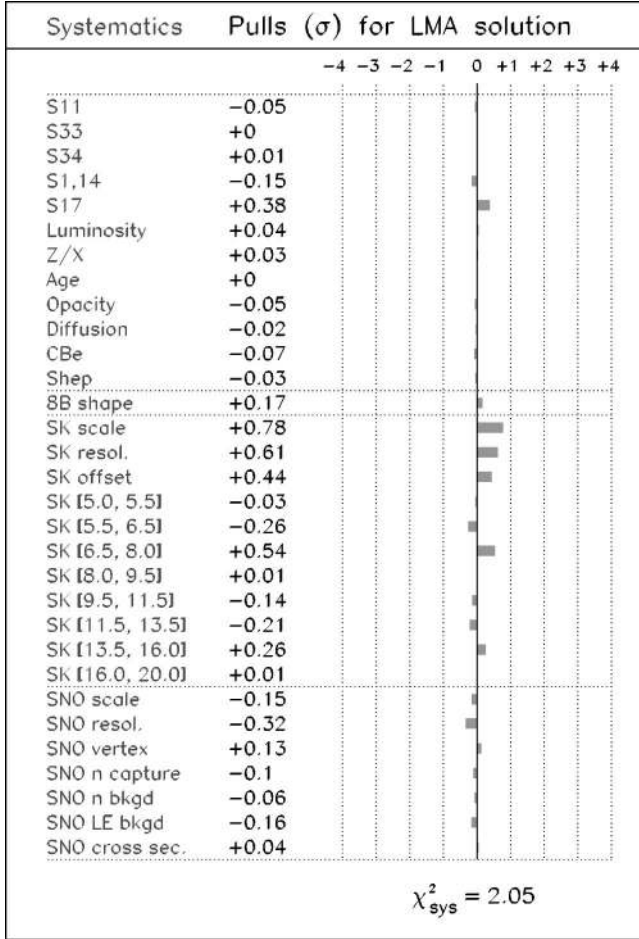


FIG. 5. Diagram of pulls  $\{\bar{\xi}_k\}_{k=1, \dots, 31}$  for correlated systematics at the LMA best-fit point. See the text for details.

where  $S$  is the inverse matrix<sup>21</sup>

$$S_{kh} = \left[ \delta_{kh} + \sum_n q_n^k q_n^h \right]^{-1}. \quad (\text{A7})$$

It turns out that the matrix  $S$  is also related to the inversion of the covariance matrix,

$$\left[ \delta_{nm} + \sum_k q_n^k q_m^k \right]^{-1} = \delta_{nm} - \sum_{k,h=1}^K S_{kh} q_m^h q_n^k. \quad (\text{A8})$$

Indeed, the product of the above two matrices gives the unit matrix. The above equation reduces the inversion of the  $N \times N$  covariance matrix in  $\chi^2_{\text{covar}}$  to the inversion of the (generally much smaller)  $K \times K$  matrix in Eq. (A7).

The last step is to write the  $\chi^2_{\text{pull}}$  in terms of the  $\bar{\xi}_k$ 's,

$$\chi^2_{\text{pull}} = \sum_{n=1}^N \left( \Delta_n - \sum_k q_n^k \bar{\xi}_k \right)^2 + \sum_{k=1}^K \bar{\xi}_k^2, \quad (\text{A9})$$

<sup>21</sup>Here we deal only with symmetric matrices. Therefore, given a matrix equation such as  $\mathbf{A} = \mathbf{B}^{-1}$ , we can conventionally write it as  $A_{nm} = [B_{nm}]^{-1}$  without index ambiguity.

TABLE V. Separate contributions to the global  $\chi^2_{\text{sys}}$  for the various solutions reported in Table I, as obtained by grouping squared pulls from Table IV.

$k$	Systematic sources	LMA	LOW	QVO	SMA
1–13	SSM and ${}^8\text{B}$ $\nu$ shape	0.2	1.0	2.4	4.3
14–24	SK systematics	1.7	1.7	1.1	2.9
25–31	SNO systematics	0.2	1.4	2.8	6.6
1–31	All (global $\chi^2_{\text{sys}}$ )	2.1	4.1	6.3	13.8

and to substitute Eq. (A6) in Eq. (A9). Expanding the right-hand side (RHS) of Eq. (A9), and making use of Eq. (A8), one recovers the RHS of Eq. (A3), namely,

$$\chi^2_{\text{covar}} \equiv \chi^2_{\text{pull}}. \quad (\text{A10})$$

Finally, we observe that setting

$$\bar{x}_n \equiv \Delta_n - \sum_{k=1}^K q_n^k \bar{\xi}_k, \quad (\text{A11})$$

as in Eq. (8), one gets from Eq. (A9) a “diagonal” form for  $\chi^2_{\text{pull}}$ ,

$$\chi^2_{\text{pull}} = \sum_{n=1}^N \bar{x}_n^2 + \sum_{k=1}^K \bar{\xi}_k^2, \quad (\text{A12})$$

as anticipated in Eq. (10).

A different proof of the previous relations have been discussed in the context of parton distribution fitting [25], where the pull method is now routinely used [26,27].

## APPENDIX B: WINTER-SUMMER DIFFERENCE IN GALLEX-GNO

Earth matter effects can generate an observable winter-summer difference ( $R_W - R_S$ ) in the event rates measured in gallium experiments. Such a difference can be as large as  $\sim 6$  SNU around the LOW solution [39].

The GALLEX-GNO Collaboration has recently reported the measurement [4] (see also [55])

$$R_W - R_S = -11 \pm 9 \text{ SNU (GALLEX-GNO)}, \quad (\text{B1})$$

whose uncertainty is almost entirely statistical [55], all systematics being largely cancelled in the difference [56]. In our

TABLE VI. Separate contributions to the global  $\chi^2_{\text{pull}}$  for the various solutions reported in Table I.

$n$	$k$	Contributions	LMA	LOW	QVO	SMA
—	1–13	SSM and ${}^8\text{B}$ $\nu$ shape	0.2	1.0	2.4	4.3
1	—	Cl experiment	3.0	3.4	7.2	0.0
2–3	—	Ga experiments	1.7	4.7	2.3	1.5
4–48	14–24	SK experiment	42.1	44.6	38.1	46.0
49–81	25–31	SNO experiment	26.4	30.1	31.2	45.1
1–81	1–31	All (global $\chi^2$ )	73.4	83.8	81.2	96.9

TABLE VII. Fractional neutrino flux shifts from the SSM central values ( $\Delta\Phi_i/\Phi_i \times 100$ ), for the various solutions.

	pp	pep	Be	B	hep	N	O
LMA	0.0	0.0	0.5	5.2	-0.8	-1.0	-1.2
LOW	0.5	0.8	-5.5	-12.2	0.0	-8.3	-8.3
QVO	1.1	1.6	-11.5	-22.2	-1.8	-15.1	-17.0
SMA	0.9	1.3	-9.9	-24.2	+1.8	-11.4	-12.8

“pull” approach, we simply attach to  $R_W - R_S$  an uncorrelated error  $u_{WS} = 9$  SNU, with no systematics.

The definition of “Winter” and “Summer” adopted in [4,55] is slightly different from the astronomical one,<sup>22</sup> and corresponds to

$$\text{“Winter”} = \text{perihelion (5 Jan.)} \pm 3 \text{ months,} \quad (\text{B2})$$

$$\text{“Summer”} = \text{aphelion (5 July)} \pm 3 \text{ months.} \quad (\text{B3})$$

Therefore, the solar exposure functions for the above periods, as shown in Fig. 7 in terms of the nadir angle ( $\eta$ ), are slightly different from the ones given in [39]. In particular, the comparison of Fig. 7 in this paper with Fig. 5 in [39] shows that the above definitions lead to a lower (higher) exposure of the innermost trajectories in the mantle during winter (summer). The total annual exposure is, of course, unaltered.

The definitions in Eqs. (B2) and (B3) are particularly useful to smoothly extend the theoretical calculation of  $R_W - R_S$  from the matter-enhanced regime [39] down to the vacuum oscillation regime, where seasonal variations are instead induced by the eccentricity variations of the orbital distance  $L$  (purely geometrical ( $1/L^2$ ) effects being factored out). Indeed, with the definitions in Eqs. (B2) and (B3), the winter-summer rate difference in vacuum happens to coincide with the near-far rate difference ( $R_N - R_F$ ) previously defined in [57]. We have then matched the results found in [39] and in [57], by considering both matter-induced and eccentricity-induced contributions to  $R_W - R_S$ , so as to calculate this quantity in the *whole* oscillation parameter space. The match between the matter and vacuum regimes occurs in the quasivacuum range, and is made easier by the lucky circumstance that Earth matter effects vanish just when the oscillating terms in the  $\nu_e$  survival probability start to be important [48].

The datum in Eq. (B1) is compatible with no seasonal asymmetry, adds a slight penalty to the region roughly corresponding to the LOW solution (where  $0 \leq R_W - R_S \leq 6$  SNU), and modulates the likelihood of the solutions in the (Q)VO regime, where both positive and negative values of the asymmetry can occur ( $-26 \leq R_W - R_S \leq +26$  SNU), the negative ones being slightly favored by the GALLEX-

<sup>22</sup>Winter and summer were defined in [39] as six-months intervals separated by equinoxes and centered, respectively, at the winter solstice (21 Dec) and at the summer solstice (21 Jun).

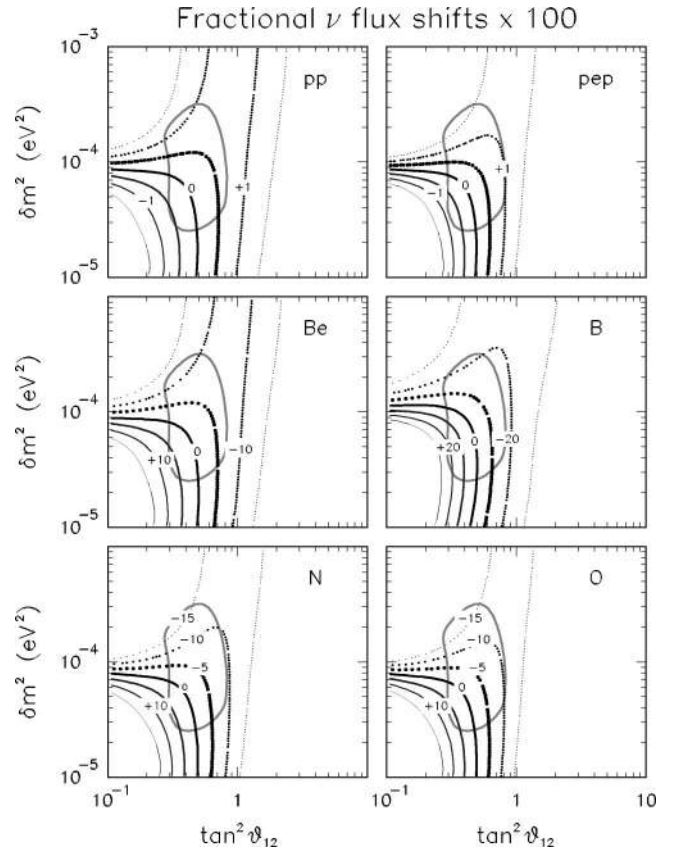


FIG. 6. Preferred deviations of the solar  $\nu$  fluxes from their SSM central values [41], in the region of the LMA solution (superposed at 99% C.L.). Dotted (solid) isolines roughly correspond to a slightly “cooler” (hotter) Sun. See the text for details.

GNO datum. We remark that (positive or negative) seasonal effects in gallium experiments, being largely driven by low-energy solar neutrino components, can be compatible with the nonobservation of ( $^8\text{B}$ -driven) seasonal effects in SK [54].

Finally, we mention that the SAGE experiment has recently reported  $\nu$  event rates in gallium, grouped in (bi)monthly intervals [2], which appear to be consistent with no seasonal variations (although no explicit  $R_W - R_S$  estimate is given in [2]). Taking the data in [2] at face value, we argue a slightly positive value for  $R_W - R_S$  in SAGE, with a total uncertainty comparable to that of GALLEX-GNO. The combination of a slightly positive (SAGE) and a slightly negative (GALLEX-GNO) winter-summer difference would then provide a central value closer to zero for  $R_W - R_S$ , very consistent with the LMA solution [39]. An official evaluation of  $R_W - R_S$  from SAGE [to be combined with the one in Eq. (B1) from GALLEX-GNO] appears thus a desirable input for future analyses.

### APPENDIX C: THE SK ENERGY-NADIR DIFFERENTIAL SPECTRUM

The SK energy-nadir spectrum of electrons induced by neutrino elastic scattering is fundamental to constrain the solar neutrino parameter space. Therefore, we think it useful

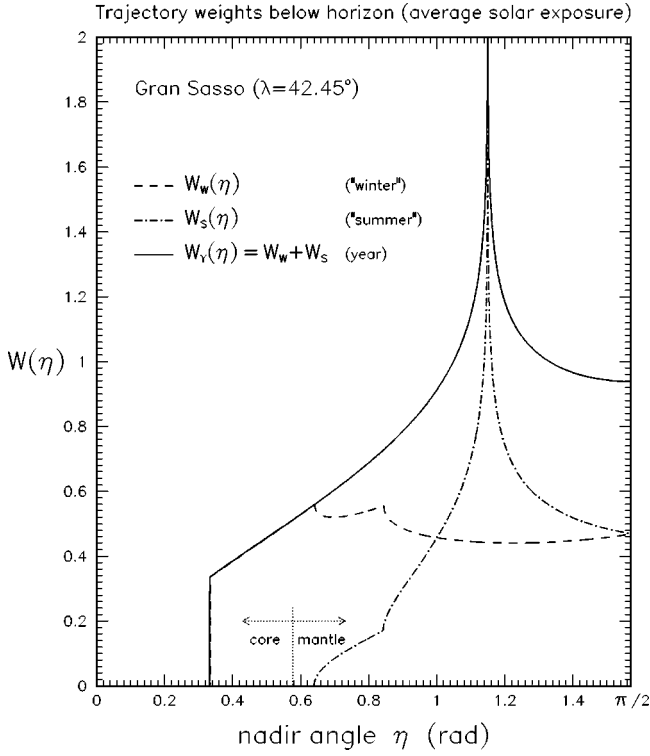


FIG. 7. Solar exposure functions (at the Gran Sasso latitude) for the “winter” and “summer” periods defined in Eqs. (B2) and (B3).

to describe in some detail our improved error estimates and theoretical calculations.

Concerning the “error format,” the pull method used in this paper does not leave any freedom in the  $\chi^2$  treatment of the spectrum, which is uniquely defined by providing, for each bin rate  $R_n$ , the uncorrelated error component  $u_n$ , and the fully correlated error components  $c_n^k$  due to independent  $k$ -th sources of systematic errors.<sup>23</sup> The task is thus reduced to a careful evaluation of such components. To reach this goal, we combine information from SK [6] and from our own evaluation of systematics.

Table VIII shows the main characteristics of the SK binned energy spectrum. The energy bins 2–7 are further divided into seven nadir angle bins [6], reported in Table IX. In each energy-nadir bin, the statistical error represents the only SK uncorrelated error component ( $u_n$ ). All other error sources in SK are correlated among bins, at least in nadir. Indeed, apart from the obvious SSM systematics, the SK bin rates are further affected by  $8 + 3 + 1 = 12$  correlated systematics, as discussed in the following.

The first eight systematic errors, listed in the fifth column of Table VIII, are uncorrelated among energy bins. In each energy bin, however, they are fully correlated in nadir [6]. Such errors represent those (nadir-independent) data reduction uncertainties which are specific of each energy bin, independently of the others.

<sup>23</sup>Therefore, we abandon our previous  $\chi^2$  approach in terms of separated SK total rate and spectral shape information [58] which, although correct, cannot be exactly cast in a “pull” form.

Three further systematics, fully correlated among all energy-nadir bins, are induced by  $^8\text{B}$   $\nu$  spectrum shape uncertainties [46] and by the SK energy scale and resolution uncertainties [6]. We note two facts. First, these sources of systematics act differently on the B and hep components in SK: for instance, the hep component is obviously unaffected by the  $^8\text{B}$  shape uncertainty.<sup>24</sup> Secondly, the relative error signs (for each source of systematics) are relevant: for instance, an increase in the energy resolution width flattens the—steeply falling—SK energy spectrum, the high-energy (low-energy) part being thus enhanced (suppressed), as evident from the eleventh and thirteenth column in Table VIII. Since the information about the relative error signs and about the separate B and hep components is not given in [6], we perform our own evaluation as follows.

The  $^8\text{B}$  spectrum shape error is evaluated by attaching to the default neutrino spectrum [47] the  $\pm 1\sigma$  shape perturbations evaluated in [46], and calculating the corresponding fractional variations in the absolute rates.<sup>25</sup> The energy scale uncertainty is evaluated by shifting the centroid of the (Gaussian) energy resolution function by 0.64% [6], namely, by taking  $T' \rightarrow T'(1 + 0.0064)$ , where  $T'$  is the true electron kinetic energy (the quantity calibrated in SK). The resolution uncertainty is evaluated by perturbing the energy resolution width  $\sigma_T$  [see Eq. (E3)] by 2.5% [6],  $\sigma_T \rightarrow \sigma_T(1 + 0.025)$ . In all cases, the same uncertainties are calculated for opposite perturbations, and small error asymmetries are averaged. The results are given in the last five columns of Table VIII, where the contributions from  $\Phi_B$  and  $\Phi_{\text{hep}}$  are separated. As far as the B flux component is concerned, there is reasonable agreement in size with the corresponding SK error evaluation in [6], except for the  $^8\text{B}$   $\nu$  spectrum shape. We are unable to explain such difference. Our error assignment is completed by an overall SK systematic offset (2.75%, symmetrized from [6]), which is attached to all energy-nadir theoretical rates with full correlation. This error mainly represents the overall uncertainty of the data reduction efficiency [54], affecting the whole spectrum.

Notice that, in Table VIII, the last eight columns refer to the no oscillation case. In the presence of oscillations, one usually updates only the theoretical rates  $R_m^{\text{theor}}$ , and assumes that the fractional errors in the last five columns are approximately unchanged. The latter assumption is a very good approximation for spectra with no or mild distortions, but is not strictly applicable in the whole oscillation parameter space. Therefore, for the sake of accuracy, in our oscillation analysis we recalculate the fractional errors in the last five col-

<sup>24</sup>Analyses where the  $\Phi_{\text{hep}}/\Phi_B$  ratio is taken as a free parameter should separately rescale the different  $\Phi_B$  and  $\Phi_{\text{hep}}$  error components in the evaluation of the total error. In fact, one cannot calculate first the total  $(\Phi_B + \Phi_{\text{hep}})$  systematic error assuming the SSM ratio for  $\Phi_{\text{hep}}/\Phi_B$ , and then use the same error when such ratio is significantly varied (say, by factors  $\sim 10$ ). We think that this remark should be taken into account, when placing upper bounds on  $\Phi_{\text{hep}}$  from the analysis of the high-energy tail of the SK spectrum.

<sup>25</sup>Conventionally, we denote as  $+1\sigma$  perturbation of the  $^8\text{B}$   $\nu$  shape the one which moves the energy spectrum to higher energies.



TABLE VIII. Characteristics of the SK energy spectrum. The first two columns define the bins in terms of observed total electron energy  $E$ . The third column is the ratio of the SK observed event rates to the SSM [41] predictions, as taken from [6], with a slight correction to account for our default hep  $\nu$  flux [we take  $\Phi_{\text{hep}}=8.3$  rather than  $9.3$  [41] in units of  $\times 10^3 \text{ cm}^{-2} \text{ s}^{-1}$ ; see Eq. (15)]. The boron flux is  $\Phi_B=5.05 \times 10^6 \text{ cm}^{-2} \text{ s}^{-1}$  [41], as in [6]. The fourth column gives the fractional uncorrelated error in each bin, whose only component is the statistical error (taken from [6]). The fifth column represents those fractional systematic errors which are uncorrelated among energy bins, but correlated in nadir bins (from [6]). The sixth, seventh and eighth columns represent our evaluation of the total, boron, and hep  $\nu$  event rate in SK (in the absence of oscillation), for 1 kton year (kty) exposure. The ninth, tenth, and eleventh column represent our evaluation of the three main systematic effects (given as  $1\sigma$  fractional contributions to  $R_m^{\text{theor}}$ ) which are fully correlated in energy and in nadir, and are generated by uncertainties in the  $^8\text{B}$   $\nu$  energy shape, SK energy scale, and SK resolution width. The last two uncertainties also affect the hep contribution to the total rate, as reported in the last two columns (our evaluation, given as  $1\sigma$  fractional contributions to  $R_{m,\text{hep}}^{\text{theor}}$ ). Finally, we attach an overall systematic offset  $c^{\text{off}} \approx 2.75\%$  [6] to all binned rates  $R_m^{\text{theor}}$ , with full correlation in energy and nadir. In the presence of oscillations, the last eight columns (properly separated into nadir bins) are recalculated for each  $(\delta m^2, \tan^2 \theta_{12})$  point.

Bin $m$	$E$ range (MeV)	$R_m^{\text{expt}}/R_m^{\text{theor}}$ (B+hep)	$u_m/R_m^{\text{expt}}$ $\times 100$	$c_m^{\text{bin}}/R_m^{\text{theor}}$ $\times 100$	$R_m^{\text{theor}^a}$ (1/kty)	$R_{m,B}^{\text{theor}}$ (1/kty)	$R_{m,\text{hep}}^{\text{theor}}$ (1/kty)	$100 \times c_{m,B}/R_{m,B}^{\text{theor}}$			$100 \times c_{m,\text{hep}}/R_{m,\text{hep}}^{\text{theor}}$	
								$^8\text{B}$ shape	Scale	Resol.	Scale	Resol.
1	[5.0,5.5]	0.4672	8.65	3.24	81.795	81.624	0.171	0.52	-0.07	-0.19	-0.38	-0.09
2	[5.5,6.5]	0.4581	3.08	1.43	140.974	140.654	0.320	0.69	0.14	-0.20	-0.29	-0.11
3	[6.5,8.0]	0.4730	1.78	1.37	155.433	155.014	0.419	1.05	0.58	-0.20	-0.09	-0.15
4	[8.0,9.5]	0.4601	2.02	1.37	95.577	95.239	0.338	1.61	1.32	-0.09	0.24	-0.18
5	[9.5,11.5]	0.4630	2.23	1.37	60.011	59.688	0.323	2.48	2.50	0.00	0.78	-0.19
6	[11.5,13.5]	0.4626	3.64	1.37	18.197	18.004	0.193	3.87	4.50	1.59	1.67	-0.07
7	[13.5,16.0]	0.5683	6.88	1.37	3.768	3.660	0.108	5.82	7.47	4.51	3.14	0.42
8	[16.5,20.0]	0.5637	26.3	1.37	0.245	0.212	0.033	8.09	12.32	11.26	6.09	2.41

<sup>a</sup>The total event rate  $R^{\text{theor}}$  is here normalized to the efficiency-corrected, no-oscillation value of 556 events/kty, as graphically derived from [59], with a correction for the updated SSM  $\Phi_{B,\text{hep}}$  values. This specific value for  $R^{\text{theor}}$  is unimportant in practice, as far as the ratios in the 3rd column are used in the analysis.

umns of Table VIII, for any  $(\delta m^2, \tan^2 \theta_{12})$  grid point (and for any nadir bin). This improvement leads to minimal differences in the local  $\chi^2_{\text{pull}}$  minima (corresponding to almost undistorted spectra), but is not totally negligible in deriving the borders of, say, the 99.73% C.L. allowed regions, where it can lead to  $|\Delta \chi^2| \approx 1$  differences.

Concerning the calculations of the  $\nu_e$  survival probability, we compute Earth matter effects [60] through eight relevant shells of the preliminary reference earth model (PREM) [61], namely (in the language of [61]): (1) ocean; (2,3) crust layers; (4) LID + low velocity zone; (5) transition zone; (6) lower mantle + D-zone; (7) outer core; and (8) inner core. In

TABLE IX. Fractional contributions to the total event rate ( $R/R_{\text{tot}}$ , our evaluation), in the case of no oscillation, from each of the seven SK nadir intervals, identified as “day” bin, “mantle” bins (M1–M5), and “core” bin. The observed SK event rates in each energy-nadir bin, together with their statistical errors, are reported in [6].

Nadir bin	$\cos \eta$ range	$R/R_{\text{tot}}$
Day	[-1,0]	0.5000
M1	[0,0.16]	0.0685
M2	[0.16,0.33]	0.0777
M3	[0.33,0.50]	0.0984
M4	[0.50,0.67]	0.1025
M5	[0.67,0.84]	0.0839
Core	[0.84,1]	0.0690
Day+Night	[-1,1]	1.0000

each of them, we approximate the radial density profile through a biquadratic parametrization, which allows a fast and accurate analytical calculation of the relevant transition probabilities in the Earth [60].

In the (quasi)vacuum oscillation regime, the oscillating term in the  $\nu_e$  survival probability  $P_{ee}$  depends implicitly upon the daily time through the orbital distance  $L(\tau_d)$ , where  $\tau_d = 2\pi \cdot \text{day}/365$ , with  $\tau_d = 0$  at winter solstice.<sup>26</sup> As noticed in [62], the different exposure of the “day” and “night” bins in terms of  $\tau_d$  induces a slight day-night vacuum difference in the time-averaged  $P_{ee}$ . Concerning the SK energy-nadir spectrum, we take into account the different exposures  $E(\eta_1, \eta_2)$  for each nadir bin range  $[\eta_1, \eta_2]$  in Table IX as follows. In a given day of the year ( $\tau_d$ ), the  $\eta$  range spanned by a detector at latitude  $\lambda$  (equal to  $36.48^\circ$  for SK) is  $[\eta_{\text{min}}(\tau_d), \eta_{\text{max}}(\tau_d)]$ , where  $\eta_{\text{min}}(\tau_d) = \lambda + \delta_S(\tau_d)$ , and  $\eta_{\text{max}}(\tau_d) = \pi - \lambda + \delta_S(\tau_d)$ , having defined the solar declination  $\delta_S(\tau_d)$  through  $\sin \delta_S = -\sin i \cos \tau_d$ , with  $\sin i = 0.3978$  (inclination of Earth axis). The daily exposure function  $E$  for a generic  $[\eta_1, \eta_2]$  nadir bin is then

$$E(\tau_d, \eta_1, \eta_2) = [\tau_h(\tau_d, \min\{\eta_2, \eta_{\text{max}}\}) - \tau_h(\tau_d, \max\{\eta_1, \eta_{\text{min}}\})] / \pi, \quad (\text{C1})$$

where  $\tau_h(\tau_d, \eta)$  is the hourly time (normalized to  $2\pi$  and

<sup>26</sup>The purely geometrical  $1/L^2(\tau_d)$  variation is assumed to be already corrected for in the SK data.

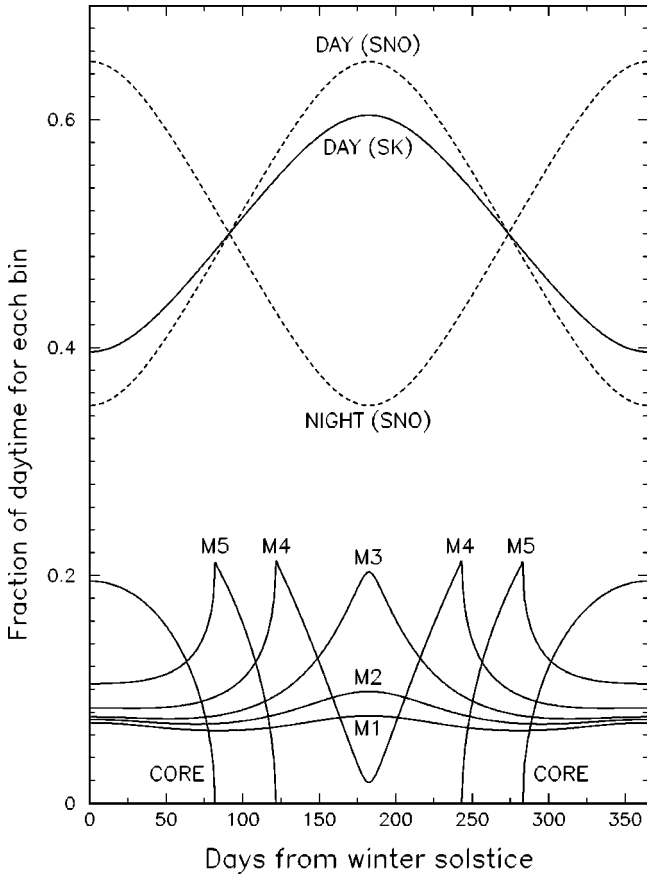


FIG. 8. Daytime solar exposures of each SK nadir bin and of the SNO day and night bins. These exposure functions are used for accurate time averages of the oscillating terms in the (quasi)vacuum regime.

starting at midnight) corresponding to the angle  $\eta$  during the day  $\tau_d$ ,<sup>27</sup>

$$\tau_h(\tau_d, \eta) = \arccos\left(\frac{\cos \eta}{\cos \lambda \cos \delta_S} + \tan \lambda \tan \delta_S\right). \quad (\text{C2})$$

Figure 8 shows the exposure functions  $E(\tau_d)$  for the seven SK nadir bins listed in Table IX, as well as for the SNO day and night bins (the functions sum up to unity in both cases). It can be seen, as intuitively expected, that the SK core bin is sensitive only to extreme values of  $L(\tau_d)$  (close to the orbital perihelion and aphelion), while the two outermost mantle bins (M1 and M2) are almost equally sensitive to all values of  $L(\tau_d)$ , being crossed by solar neutrinos during the whole year. We take into account the different bin exposures in Fig. 8 when time-averaging the oscillating terms in the (quasi)vacuum regime, for both SK and SNO.

The results of our oscillation analysis of the SK spectrum are given in the SK panel of the (previously discussed) Fig. 2. The C.L. contours compare well with the official SK ones,

<sup>27</sup>Any angle  $\eta \in [\eta_{\min}, \eta_{\max}]$  is spanned twice each day. This explains the appearance of  $\pi$  (rather than of  $2\pi$ ) in the denominator of Eq. (C1).

as reported in Fig. 2 of [6] (we also obtain very good agreement for the normalization-free case, not shown).

A final remark is in order. All the SK systematic error sources discussed in [6] (and adopted in this work) are fully correlated in nadir. This means that no allowance is given in [6] for uncorrelated nadir shape variations, apart from the obvious statistical fluctuations. However, it is known from previous SK publications [22,63] and presentations [59] that some systematics *do not* cancel in day-night differences, and may thus, in general, affect the nadir bins in uncorrelated ways. In addition, Earth matter density and chemical composition uncertainties may also contribute to small (and different) errors [64,65] in the various nadir bins [66] via  $\nu_e$  regeneration effects. In particular, one should not forget that the widely used PREM model is spherically symmetric by construction, and that local departures from the world-averaged density are to be expected. For instance, the first half of the SK mantle bin M1 (see Table IX) is sensitive to the PREM “ocean+crust” density, whose local characteristics at the SK site may well be different from the world average. The inclusion of such additional uncertainties might give a little more freedom to fit possible distortions in the nadir distributions. Therefore, if the (currently weak) hints for an excess of night events in SK [54] and in SNO [9] will be corroborated by future data, an improved discussion of the nadir spectrum uncertainties will be useful to precisely assess their statistical significance.

#### APPENDIX D: TREATMENT OF THE SNO DAY-NIGHT ENERGY SPECTRUM

The solar neutrino events observed in the SNO spectrum [8] cannot be currently identified as being of ES, CC, or NC type on an event-by-event basis. A statistical separation is possible, however, by exploiting their different distribution in terms of suitable variables, the most important being the observed (effective) electron kinetic energy  $T$ . Since the ES and CC distribution shapes in  $T$  depend upon the oscillation parameters, also the inferred CC and NC rates depend on such parameters, as stressed in [40].

In the oscillation analysis, however, it is not necessary to perform a separate fit to the ES, CC, and NC components as done in [18]. Given the oscillated predictions for these components, one can simply add them up (together with the known background rates) in each energy bin, calculate the corresponding systematics, and fit the observed SNO day-night energy spectrum. This method, which has been dubbed “forward fitting” by the SNO Collaboration [40], allows us to take into account the full spectral information (central values and errors of each bin). In the following, we describe our implementation of such method in the  $\chi^2_{\text{pull}}$  evaluation.

Table X reports some relevant characteristics of the SNO spectrum, including our evaluation of the SNO neutrino signal components and their errors (small error asymmetries being averaged out). The effects of the  $^8\text{B}$   $\nu$  spectrum shape error (not included in the official SNO analysis [8,9]) are estimated as in SK (see Appendix C). Notice that a  $+1\sigma$  shift of this systematic uncertainty increases the number of signal events, especially at high energies. The fractional in-

TABLE X. Characteristics of the SNO spectrum, divided in 17 day and 17 night bins (first two columns). The experimental rates [8] are given in the third and fourth columns, and include signal (CC+ES+NC) and background events. Our evaluation for the corresponding CC, ES, and NC components and of their  $^8\text{B}$   $\nu$  shape, energy scale and resolution errors (in the absence of oscillation, day+night) are given in the remaining 12 columns. The NC signal is negligible in the last 8 bins. All the quoted numbers refer to the total  $\Phi_B + \Phi_{\text{hep}}$  contributions. In the analysis, however, the  $\Phi_B$  and  $\Phi_{\text{hep}}$  contributions and their errors are separately evaluated, analogously to the SK spectrum. In the presence of oscillations, the last twelve columns are split into day and night contributions and updated in each point of the parameter space. Backgrounds are oscillation-independent and are treated according to [40].

Bin <i>m</i>	<i>T</i> range (MeV)	$R_{\text{day}}^{\text{expt}}$ (1/kty)	$R_{\text{night}}^{\text{expt}}$ (1/kty)	$R_{\text{CC}}^{\text{theor}}$ (1/kty)	fractional errors $\times 100$			$R_{\text{ES}}^{\text{theor}}$ (1/kty)	fractional errors $\times 100$			$R_{\text{NC}}^{\text{theor}}$ (1/kty)	fractional errors $\times 100$		
					Shape	Scale	Resol.		Shape	Scale	Resol.		Shape	Scale	Resol.
1	[5,5.5]	351.1	399.7	822.2	0.42	-2.30	0.10	135.8	0.64	0.26	-0.26	293.8	1.55	0.88	-4.33
2	[5.5,6]	330.9	313.4	875.6	0.63	-1.89	-0.21	121.7	0.77	0.57	-0.35	248.5	1.55	3.73	-2.84
3	[6,6.5]	299.6	272.2	903.0	0.86	-1.40	-0.53	107.8	0.91	0.93	-0.46	172.1	1.55	7.05	0.43
4	[6.5,7]	222.4	249.6	902.0	1.12	-0.85	-0.83	94.1	1.07	1.32	-0.54	97.7	1.55	10.85	5.43
5	[7,7.5]	191.2	235.0	872.8	1.41	-0.22	-1.09	81.0	1.24	1.77	-0.58	45.4	1.55	15.16	12.18
6	[7.5,8]	148.9	176.6	817.7	1.73	0.51	-1.30	68.7	1.44	2.28	-0.58	17.3	1.55	19.96	20.68
7	[8,8.5]	128.7	122.1	740.9	2.08	1.33	-1.42	57.2	1.66	2.85	-0.54	5.4	1.55	25.26	31.02
8	[8.5,9]	139.7	134.1	648.5	2.47	2.25	-1.41	46.9	1.90	3.48	-0.43	1.4	1.55	31.19	43.38
9	[9,9.5]	90.1	95.6	547.4	2.89	3.29	-1.24	37.7	2.16	4.19	-0.23	0.3	1.55	37.69	58.11
10	[9.5,10]	82.7	86.3	444.9	3.36	4.45	-0.85	29.6	2.45	4.99	0.07	0	—	—	—
11	[10,10.5]	66.2	62.4	347.5	3.86	5.74	-0.18	22.8	2.77	5.87	0.51	0	—	—	—
12	[10.5,11]	49.6	59.8	260.4	4.40	7.16	0.82	17.1	3.12	6.86	1.13	0	—	—	—
13	[11,11.5]	31.3	41.2	186.8	4.97	8.70	2.21	12.5	3.51	7.94	1.97	0	—	—	—
14	[11.5,12]	18.4	21.2	128.2	5.56	10.37	4.04	8.9	3.92	9.14	3.07	0	—	—	—
15	[12,12.5]	9.2	18.6	84.0	6.17	12.15	6.35	6.1	4.36	10.45	4.47	0	—	—	—
16	[12.5,13]	11.0	15.9	52.6	6.79	14.01	9.13	4.1	4.83	11.87	6.23	0	—	—	—
17	[13,20]	9.2	9.3	71.1	7.68	17.83	16.34	6.5	5.97	15.71	12.48	0	—	—	—

crease is obviously constant for the NC events, which have no memory of the original  $\nu$  energy. From Table X it appears that, in the bulk of the SNO spectrum, the  $^8\text{B}$   $\nu$  shape uncertainties are not negligible as compared with the (purely instrumental) SNO energy calibration and resolution uncertainties. The latter two errors are evaluated by shifting the centroid of the energy resolution function and varying its width in the way described in Ref. [40], and calculating the corresponding variations in each bin of the CC, NC, and ES spectrum. Actually we separate the  $\Phi_B$  and  $\Phi_{\text{hep}}$  components (not shown in Table X), as for the SK spectrum. In the presence of oscillations, we not only update the day and night rates in each bin, but also their *fractional* systematic errors, for each point in the mass-mixing plane. As for SK, the effect of this improved estimate of fractional systematic errors is rather small in the local  $\chi^2$  minima, but increases towards the borders of the 99.73% C.L. regions, where the spectral distortions can be more sizeable. In the fit to SNO data only, such improvement can lead to  $\chi_{\text{pull}}^2$  variations as large as  $|\Delta\chi^2| \sim 4$  at the  $3\sigma$  borders, and is thus not totally negligible in deriving precise C.L. contours for the less favored solutions. Finally, notice that the three systematic error sources in Table X can induce, in the various bins, event rate variations with different relative signs, which are taken into account in the analysis.

Besides the previous three systematic error sources, we include a vertex reconstruction uncertainty, whose  $+1\sigma$  effect is to increase the CC and ES rates by  $+3\%$  and the NC rates by  $+1.45\%$  [40]. The CC and NC binned rates are also

affected by a systematic cross section uncertainty, whose  $+1\sigma$  effect is to increase them by  $+1.8\%$  and  $+1.3\%$ , respectively [8].<sup>28</sup> The CC and NC cross section errors embed differences between independent theoretical calculations [67,68] and uncertainties related to additional radiative corrections [69,70], as discussed in [8]. Finally, the various SNO background components [40] are affected by the so-called neutron capture, neutron background, and low-energy (LE) background correlated systematics, whose oscillation-independent effects (included in our analysis) are reported in [40] and not repeated here.

When all such inputs are included, our fit to SNO data only provides the allowed regions given in the lower right panel of Fig. 2. Such regions appear to be somewhat different from those found in Ref. [9], as discussed in Sec. IV B.

#### APPENDIX E: QUASI-MODEL-INDEPENDENT ANALYSIS OF SK AND SNO

In this last appendix we present a new version of the model-independent comparison of SK ES and SNO (CC and NC) total rates, first proposed in [71] and then applied in [58,72] to earlier SNO CC data.

For the current SNO threshold  $T_{\text{SNO}} \geq 5$  MeV [8], the SK threshold equalizing the SNO CC and SK ES response func-

<sup>28</sup>The correlation between the NC and CC cross section errors can be safely taken  $\sim 1$  in the SNO analysis.

tions [71] turns out to be  $T_{SK} \geq 6.74$  MeV, corresponding to a total electron energy  $E_{SK} \geq 7.25$  MeV,

$$\begin{aligned} & \text{SNO CC response}(T_{\text{SNO}} \geq 5 \text{ MeV}) \\ & \Leftrightarrow \text{SK ES response}(E_{SK} \geq 7.25 \text{ MeV}). \end{aligned} \quad (\text{E1})$$

In calculating the response functions, we have taken into account the latest evaluation of the energy resolution width  $\sigma_T$  in SNO [8],

$$\sigma_T(\text{SNO}) = -0.0684 + 0.331\sqrt{T'} + 0.0425 T', \quad (\text{E2})$$

where  $T'$  is the true electron kinetic energy, and both  $T'$  and  $\sigma_T$  are given in MeV. We have cast, in the same form, the latest evaluation of  $\sigma_T$  for SK (graphically reported in [23]),

$$\sigma_T(\text{SK}) = 0.25 + 0.20\sqrt{T'} + 0.06 T'. \quad (\text{E3})$$

From the spectral information discussed in Appendix C we estimate (derivation omitted)

$$\Phi_{\text{ES}}^{\text{SK}} \approx 2.35 \pm 0.029 \pm 0.080 \pm 0.045 \quad (E \geq 7.25 \text{ MeV}), \quad (\text{E4})$$

in units of  $10^6 \text{ cm}^{-2} \text{ s}^{-1}$ . In the above equation, the first error is statistical, while the second represents the (properly propagated) sum of systematic errors, with the exception of the  ${}^8\text{B}$  shape uncertainty, given separately as a third error component.

While the above SK ES flux estimate is safe for model-independent analyses, the current SNO CC flux [8] is not, since its value *does depend* on model-dependent assumptions, governing the CC spectrum distortions and thus the CC-NC separation. [40] However, we can resort to a quasi-model-independent analysis, by assuming that the only observable effect of new neutrino physics can be embedded in a shift of the first spectral moment [73], namely, in a linear distortion (tilt) of the CC energy spectrum.<sup>29</sup> This assumption is reasonably general, since the current SNO statistics is not high enough to really constrain higher moments, and since we know from SK that only the scenarios with mild distortions can survive. In this case, the normalization-preserving form of a generic linear distortion for the CC differential energy spectrum reads

$$\frac{dN_{\text{CC}}(T)}{dT} \rightarrow \frac{dN_{\text{CC}}(T)}{dT} \left( 1 + \frac{T - \langle T \rangle}{\langle T^2 \rangle - \langle T \rangle^2} \Delta \langle T \rangle \right), \quad (\text{E5})$$

where  $\langle T \rangle$  and  $\langle T^2 \rangle$  are the first and second moment of the undistorted spectrum, and  $\Delta \langle T \rangle$  is the shift in the first moment.

Assuming  $\Delta \langle T \rangle$  free, our fit to the SNO energy spectrum gives the following CC and NC fluxes,

<sup>29</sup>The numerical results for a linear distortion of the CC component of the SNO spectrum are very similar to those obtained for a linear distortion of the CC+ES components (not shown), since the ES contribution is relatively small in SNO.

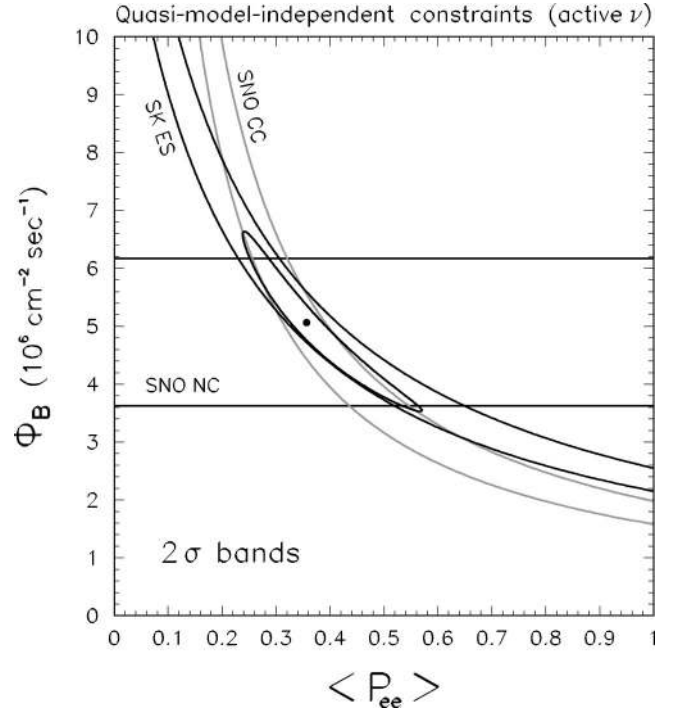


FIG. 9. Quasi-model-independent comparison of SK (ES) and SNO (CC and NC) total event rates in the plane charted by the boron flux  $\Phi_B$  and by the average  $\nu_e$  survival probability  $\langle P_{ee} \rangle$ , for equalized SK and SNO response functions. The evaluation of the SNO rates includes possible *linear* distortions in the energy spectrum. The  $2\sigma$  bands for each datum ( $\Delta\chi^2=4$ ) appear to be in very good agreement with each other for  $P_{ee} \sim 1/3$  and for  $\Phi_B$  close to its SSM prediction [41]. The combination of the  $2\sigma$  bands is also shown (slanted elliptical region).

$$\Phi_{\text{CC}}^{\text{SNO}} = 1.78 \pm 0.10(\text{stat}), \quad (\text{E6})$$

$$\Phi_{\text{NC}}^{\text{SNO}} = 4.90 \pm 0.66(\text{stat}), \quad (\text{E7})$$

with correlation  $\rho = -0.8$ . By setting  $\Delta \langle T \rangle = 0$ , we would instead obtain  $\Phi_{\text{CC}}^{\text{SNO}} = 1.73 \pm 0.06(\text{stat})$  and  $\Phi_{\text{NC}}^{\text{SNO}} = 5.29 \pm 0.43(\text{stat})$  with correlation  $\rho = -0.62$ , in good agreement with the results of [8,9] for undistorted spectrum. The larger statistical errors in Eqs. (E6) and (E7) are the price to pay to allow possible linear distortions in the fit.

Systematic errors are attached as follows. From the (positively and negatively correlated) SNO error components reported in Table II of [8], we estimate the (CC,NC) experimental systematics as (5.2%, 8.8%), with correlation  $\rho = -0.5$ . The corresponding theoretical cross section uncertainties [(1.8%, 1.3%) from Table II of [8]] are assumed to have  $\rho \approx 1$ . Finally, if we repeat to the fit leading to Eqs. (E6) and (E7) with a  $+1\sigma$  perturbed  ${}^8\text{B}$  neutrino energy spectrum, we obtain the variations (-1.1%, +3.3%), which are fully correlated among themselves and with the third SK error component in Eq. (E4).

In conclusion, we get (in units of  $10^6 \text{ cm}^{-2} \text{ s}^{-1}$ ),

$$\Phi_{\text{ES}}^{\text{SK}} = 2.35 \pm 0.10, \quad (\text{E8})$$

$$\Phi_{\text{CC}}^{\text{SNO}} = 1.78 \pm 0.14, \quad (\text{E9})$$

$$\Phi_{\text{NC}}^{\text{SNO}} = 4.90 \pm 0.80, \quad (\text{E10})$$

with correlation matrix

$$\rho = \begin{pmatrix} 1 & -0.07 & +0.09 \\ & 1 & -0.65 \\ & & 1 \end{pmatrix}. \quad (\text{E11})$$

The above SK and SNO equalized fluxes can be useful to constrain generic models of new physics (alternative to—or coexisting with—usual mass-mixing oscillations), as far as their main distortion effect on the SNO CC spectrum is approximately linear in  $T$ . Within this quasi-model-independent assumption, and in the hypothesis of active oscillations, the fluxes in Eqs. (E8)–(E10) are still linked by the *exact* relations [71].

$$\Phi_{\text{ES}}^{\text{SK}} = \Phi_B [\langle P_{ee} \rangle + r(1 - \langle P_{ee} \rangle)], \quad (\text{E12})$$

$$\Phi_{\text{CC}}^{\text{SNO}} = \Phi_B \langle P_{ee} \rangle, \quad (\text{E13})$$

$$\Phi_{\text{NC}}^{\text{SNO}} = \Phi_B, \quad (\text{E14})$$

where  $P_{ee}(E_\nu)$  is not necessarily constant in energy, and  $r = 0.154$  is the ratio of  $\nu_{\mu,\tau}$  and  $\nu_e$  CC cross sections (averaged over the current SNO equalized response function). In the above equations,  $\Phi_B$  is the true  ${}^8\text{B}$  flux from the Sun (generally different from the SSM value), and  $\langle P_{ee} \rangle$  is the energy average of  $P_{ee}(E_\nu)$  over the response function (equal in SK and SNO).

Equations (E8)–(E11) and (E12)–(E14) overconstrain the two parameters  $\Phi_B$  and  $\langle P_{ee} \rangle$ . Figure 9 shows, in  $(\Phi_B, \langle P_{ee} \rangle)$  coordinates, both separate and combined bounds at the  $2\sigma$  level for each datum ( $\Delta\chi^2=4$ ). There is very good agreement between any two out of the three data in Eqs. (E8)–(E10). Their combination strengthens previous model-independent indications [58,72] for a consistency of  $\Phi_B$  with the SSM prediction [41] and for  $\langle P_{ee} \rangle \sim 1/3$  in the SK-SNO energy range.

- 
- [1] Homestake Collaboration, B.T. Cleveland *et al.*, *Astrophys. J.* **496**, 505 (1998).
- [2] SAGE Collaboration, J.N. Abdurashitov *et al.*, astro-ph/0204245.
- [3] GALLEX Collaboration, W. Hampel *et al.*, *Phys. Lett. B* **447**, 127 (1999).
- [4] GNO Collaboration, T. Kirsten *et al.*, in *Neutrino 2002*, 20th International Conference on Neutrino Physics and Astrophysics (Munich, Germany, 2002).
- [5] Kamiokande Collaboration, Y. Fukuda *et al.*, *Phys. Rev. Lett.* **77**, 1683 (1996).
- [6] Super-Kamiokande Collaboration, S. Fukuda *et al.*, *Phys. Lett. B* **539**, 179 (2002).
- [7] SNO Collaboration, Q.R. Ahmad *et al.*, *Phys. Rev. Lett.* **87**, 071301 (2001).
- [8] SNO Collaboration, Q.R. Ahmad *et al.*, *Phys. Rev. Lett.* **89**, 011301 (2002).
- [9] SNO Collaboration, Q.R. Ahmad *et al.*, *Phys. Rev. Lett.* **89**, 011302 (2002).
- [10] J. N. Bahcall, *Neutrino Astrophysics* (Cambridge University Press, Cambridge, England, 1989).
- [11] Z. Maki, M. Nakagawa, and S. Sakata, *Prog. Theor. Phys.* **28**, 870 (1962); B. Pontecorvo, *Zh. Éksp. Teor. Fiz.* **53**, 1717 (1968) [*Sov. Phys. JETP* **26**, 984 (1968)].
- [12] L. Wolfenstein, *Phys. Rev. D* **17**, 2369 (1978); S.P. Mikheev and A.Yu. Smirnov, *Yad. Fiz.* **42**, 1441 (1985) [*Sov. J. Nucl. Phys.* **42**, 913 (1985)]; V.D. Barger, K. Whisnant, S. Pakvasa, and R.J. Phillips, *Phys. Rev. D* **22**, 2718 (1980).
- [13] KamLAND Collaboration, J. Shirai *et al.*, in *Neutrino 2002* [4].
- [14] BOREXINO Collaboration, G. Bellini *et al.*, in *Neutrino 2002* [4].
- [15] V. Barger, D. Marfatia, K. Whisnant, and B.P. Wood, *Phys. Lett. B* **537**, 179 (2002).
- [16] P. Creminelli, G. Signorelli, and A. Strumia, *J. High Energy Phys.* **05**, 052 (2001).
- [17] A. Bandyopadhyay, S. Choubey, S. Goswami, and D.P. Roy, *Phys. Lett. B* **540**, 14 (2002).
- [18] J.N. Bahcall, M.C. Gonzalez-Garcia, and C. Pena-Garay, hep-ph/0204314.
- [19] P.C. de Holanda and A.Yu. Smirnov, hep-ph/0205241.
- [20] A. Strumia, C. Cattadori, N. Ferrari, and F. Vissani, hep-ph/0205261.
- [21] G.L. Fogli and E. Lisi, *Astropart. Phys.* **3**, 185 (1995).
- [22] Super-Kamiokande Collaboration, S. Fukuda *et al.*, *Phys. Rev. Lett.* **86**, 5656 (2001).
- [23] M.B. Smy, in *NOON 2001*, 3rd Workshop on Neutrino Oscillations and their Origin (Kashiwa, Japan, 2001). See also the transparencies at [www-sk.icrr.u-tokyo.ac.jp/noon2001](http://www-sk.icrr.u-tokyo.ac.jp/noon2001).
- [24] A. Strumia and F. Vissani, *J. High Energy Phys.* **11**, 048 (2001).
- [25] D. Stump *et al.*, *Phys. Rev. D* **65**, 014012 (2002).
- [26] M. Botje, *J. Phys. G* **28**, 779 (2002).
- [27] J. Pumplin, D.R. Stump, J. Huston, H.L. Lai, P. Nadolsky, and W.K. Tung, *J. High Energy Phys.* **07**, 012 (2002).
- [28] R.S. Thorne, talk at Conference on Advanced Statistical Techniques in Particle Physics (Durham, England, 2002), hep-ph/0205235.
- [29] S.L. Bridle, A. Crittenden, A. Melchiorri, M.P. Hobson, R. Kneissl, and A.N. Lasenby, astro-ph/0112114.
- [30] LEP ElectroWeak Working Group documentation, available at [lepewwg.web.cern.ch/LEPEWWG](http://lepewwg.web.cern.ch/LEPEWWG). See also hep-ex/0112021.
- [31] P. Huber, M. Lindner, and W. Winter, hep-ph/0204352.
- [32] P.I. Krastev and A.Y. Smirnov, *Phys. Rev. D* **65**, 073022 (2002).
- [33] J.N. Bahcall, M.C. Gonzalez-Garcia, and C. Pena-Garay, hep-ph/0204194.
- [34] M.V. Garzelli and C. Giunti, *Phys. Lett. B* **488**, 339 (2000).

- [35] V.D. Barger, R.J. Phillips, and K. Whisnant, *Phys. Rev. D* **43**, 1110 (1991).
- [36] C.M. Bhat, P.C. Bhat, M. Paterno, and H.B. Prosper, *Phys. Rev. Lett.* **81**, 5056 (1998).
- [37] G.L. Fogli, E. Lisi, D. Montanino, and A. Palazzo, *Phys. Rev. D* **62**, 013002 (2000).
- [38] J.N. Bahcall, *Phys. Rev. C* **56**, 3391 (1997).
- [39] G.L. Fogli, E. Lisi, D. Montanino, and A. Palazzo, *Phys. Rev. D* **61**, 073009 (2000).
- [40] SNO Collaboration, "HOWTO use the SNO Solar Neutrino Spectral data," available at [owl.phy.queensu.ca/sno/prlwebpage](http://owl.phy.queensu.ca/sno/prlwebpage).
- [41] J.N. Bahcall, M.H. Pinsonneault, and S. Basu, *Astrophys. J.* **555**, 990 (2001).
- [42] T.S. Park *et al.*, [nucl-th/0107012](http://nucl-th/0107012); see also L.E. Marcucci *et al.*, *Phys. Rev. Lett.* **84**, 5959 (2000); L.E. Marcucci *et al.*, *Phys. Rev. C* **63**, 015801 (2001).
- [43] V. Castellani, S. Degl'Innocenti, G. Fiorentini, M. Lissia, and B. Ricci, *Phys. Rep.* **281**, 309 (1997).
- [44] J.N. Bahcall, *Phys. Rev. C* **65**, 025801 (2002).
- [45] J.N. Bahcall and A. Ulmer, *Phys. Rev. D* **53**, 4202 (1996).
- [46] J.N. Bahcall, E. Lisi, D.E. Alburger, L. De Braeckeleer, S.J. Freedman, and J. Napolitano, *Phys. Rev. C* **54**, 411 (1996).
- [47] C.E. Ortiz, A. Garcia, R.A. Waltz, M. Bhattacharya, and A.K. Komives, *Phys. Rev. Lett.* **85**, 2909 (2000).
- [48] G.L. Fogli, E. Lisi, D. Montanino, and A. Palazzo, *Phys. Rev. D* **62**, 113004 (2000).
- [49] E. Lisi, A. Marrone, D. Montanino, A. Palazzo, and S.T. Petcov, *Phys. Rev. D* **63**, 093002 (2001).
- [50] Particle Data Group, D.E. Groom *et al.*, *Eur. Phys. J. C* **15**, 1 (2000).
- [51] J.C. Collins and J. Pumplin, [hep-ph/0105207](http://hep-ph/0105207).
- [52] L. Lyons, "Selecting between two hypotheses," Oxford University Report No. OUNP-99-12.
- [53] CHOOZ Collaboration, M. Apollonio *et al.*, *Phys. Lett. B* **466**, 415 (1999).
- [54] M. Smy, in *Neutrino 2002* [4].
- [55] GALLEX-GNO Collaboration, C.M. Cattadori *et al.*, in *TAUP 2001, 7th International Workshop on Topics in Astroparticle and Underground Physics* (Assergi, Italy, 2001) [*Nucl. Phys. B* (Proc. Suppl.) **110**, 311 (2002)].
- [56] C.M. Cattadori (private communication).
- [57] B. Faïd, G.L. Fogli, E. Lisi, and D. Montanino, *Phys. Rev. D* **55**, 1353 (1997).
- [58] G.L. Fogli, E. Lisi, D. Montanino, and A. Palazzo, *Phys. Rev. D* **64**, 093007 (2001).
- [59] Y. Fukuda for the SK Collaboration, talk at *NuFACT 2001*, 3rd International Workshop on Neutrino Factories based on Muon Storage Rings. Slides available at [psux1.kek.jp/~nufact01](http://psux1.kek.jp/~nufact01).
- [60] E. Lisi and D. Montanino, *Phys. Rev. D* **56**, 1792 (1997).
- [61] A.M. Dziewonsky and D.L. Anderson, *Phys. Earth Planet. Inter.* **25**, 297 (1981).
- [62] J.N. Bahcall, P.I. Krastev, and A.Y. Smirnov, *Phys. Rev. D* **62**, 093004 (2000); **63**, 053012 (2001).
- [63] Super-Kamiokande Collaboration, S. Fukuda *et al.*, *Phys. Rev. Lett.* **86**, 5651 (2001).
- [64] J.N. Bahcall and P.I. Krastev, *Phys. Rev. C* **56**, 2839 (1997).
- [65] M. Maris and S.T. Petcov, *Phys. Rev. D* **56**, 7444 (1997).
- [66] L.-Y. Shan and X.-M. Zhang, *Phys. Rev. D* **65**, 113011 (2002).
- [67] S. Nakamura, T. Sato, V. Gudkov, and K. Kubodera, *Phys. Rev. C* **63**, 034617 (2001).
- [68] M. Butler, J.-W. Chen, and X. Kong, *Phys. Rev. C* **63**, 035501 (2001).
- [69] J.F. Beacom and S.J. Parke, *Phys. Rev. D* **64**, 091302(R) (2001); see also I.S. Towner, *Phys. Rev. C* **58**, 1288 (1998).
- [70] A. Kurylov, M.J. Ramsey-Musolf, and P. Vogel, *Phys. Rev. C* **65**, 055501 (2002).
- [71] F.L. Villante, G. Fiorentini, and E. Lisi, *Phys. Rev. D* **59**, 013006 (1999).
- [72] G.L. Fogli, E. Lisi, D. Montanino, and A. Palazzo, *Phys. Rev. D* **65**, 117301 (2002).
- [73] J.N. Bahcall and E. Lisi, *Phys. Rev. D* **54**, 5417 (1996); J.N. Bahcall, P.I. Krastev, and E. Lisi, *Phys. Rev. C* **55**, 494 (1997).